

MASTER THESIS

**Tetraquark bound states in a
Bethe-Salpeter approach**

WALTER HEUPEL*

28. September 2011

INSTITUTE FOR THEORETICAL PHYSICS I
JUSTUS-LIEBIG-UNIVERSITÄT GIESSEN

*E-Mail: walter.heupel@physik.uni-giessen.de

Table of contents

1	Introduction and motivation	1
2	Quantum chromodynamics and Dyson–Schwinger equations	6
2.1	Quark DSE	10
2.2	Effective gluon	12
2.3	Solving the quark DSE	13
2.4	Solving the quark DSE for complex momenta	16
3	Mesons and diquarks	19
3.1	Two-body equation	19
3.2	Structure of the bound-state amplitudes	21
3.3	Meson amplitudes	23
3.4	Diquark amplitudes	25
3.5	Structure of offshell diquark and meson amplitudes	27
3.6	Diquark and meson propagators	28
3.7	Results for the meson and diquark BSEs	30
4	Tetraquarks	32
4.1	Four-body equations	32
4.2	Diagrammatic derivation	37
4.3	Four-body kernels	41
4.3.1	Meson-meson kernel	43
4.3.2	Meson-diquark kernel	44
4.3.3	Diquark-meson kernel	45
4.4	Prefactors in the tetraquark BSE	47
5	Numerics	51
5.1	The BSE as eigenvalue problem	51
5.2	Smolyak Integration	53
6	Results	56

7	Conclusions and outlook	62
8	Appendix	64
8.1	Chebyshev polynomials	64
8.2	Euclidean conventions	64
9	Acknowledgements	66
	Bibliography	67

Hiermit erkläre ich an Eides statt, das ich die vorliegende Master-These selbstständig,
unter Verwendung der angegebenen Quellen und ohne weitere Hilfsmittel verfasst habe.

Herborn, den 28. September 2011

Walter Heupel

1 Introduction and motivation

In the 60's, quarks were introduced as building blocks of the strong interaction [1] and provided a tool to explain the numerous particles in the observed hadron spectrum. In this picture, hadrons, a synonym for strongly interacting particles, are viewed as bound-states of valence quarks. The different valence quark content is used to characterize the bound states and the following classification was found to explain the observed spectrum very well: particles that consist of a quark (q) and an antiquark (\bar{q}) are called mesons and their quark content is denoted as $(q\bar{q})$; particles that are built up by three quarks are called baryons and their quark content reads (qqq) .

With the quarks as new fundamental particles, also two new quantum numbers were introduced. They were called color and flavor. There are three different 'colors' and the underlying group structure is therefore $SU(3)$. Because no single quark was observed and only colorless hadrons were experimentally found, the concept of confinement was introduced. Put in simple words, this concept states that all observable particles are colorless. Up to now, no violation of this conjecture was found experimentally.

The flavor quantum number can take six different values, called u(p), d(own), s(trange), c(harm), b(ottom) and t(op). Different from the color quantum number, the flavor symmetry is explicitly broken and quarks with different flavors have different masses. The u quark ($m_u \approx 3$ MeV), d quark ($m_d \approx 5$ MeV) and s quark ($m_s \approx 100$ MeV) are much lighter than the other three quarks which have masses well above 1 GeV. This gave rise to use $SU(3)$ as flavor group structure to describe the lower-mass hadron spectrum. A combination of a quark and antiquark in a $SU(3)$ flavor representation produces a nonet multiplet structure, which can be inferred from the tensor product decomposition: $(3 \otimes \bar{3}) = (8 \oplus 1)$. Thus, the nonet structure is a fundamental consequence of the $(q\bar{q})$ picture.

The different nonets of the $(q\bar{q})$ picture are classified by the total angular momentum J , the parity (P) and the charge-conjugation symmetry (C). As usual, the notation reads $J^{P(C)}$. For example, the $1^{(-)}$ $(q\bar{q})$ -nonet is depicted in Fig. 1.1. By looking at the quark-content, the state with the lowest mass is expected to be the iso-triplet ρ^0, ρ^+, ρ^- , and K^* and ϕ are expected to be heavier because of their strange-quark content. Indeed,

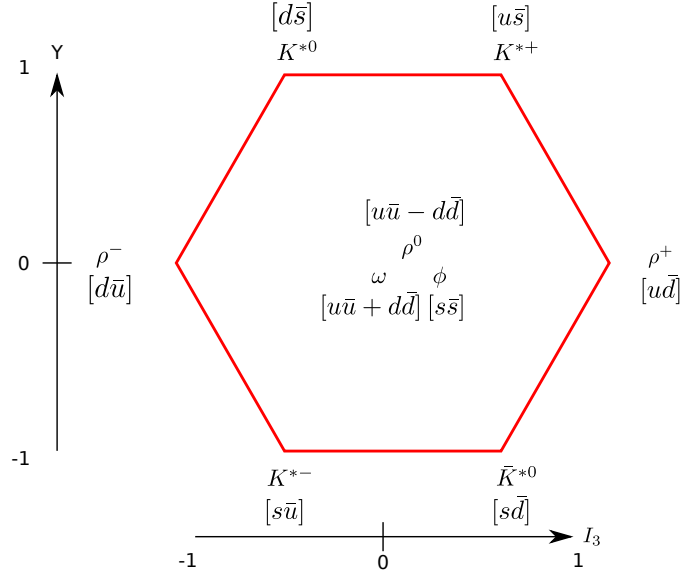


Figure 1.1: The $1^{(-)}$ meson nonet. The vertical axis denotes the hypercharge $Y = 2Q - 2I_3$, I_3 the isospin and Q the electrical charge.

this is the case and the ρ mesons are the lightest ones in this nonet ($m_\pi \approx 775$ MeV) and the K^* s and the ϕ are much heavier ($m_{K^*} \approx 890$ MeV, $m_\phi \approx 1019$ MeV).

However, not all observed hadrons are compatible with the $q\bar{q}$ picture. A prominent example is the 0^{++} state. Before going into detail why a $(q\bar{q})$ description of this state does not explain the observed particles, some remarks on the experimental status on the 0^{++} nonet are given.

The lowest-lying states with the quantum numbers 0^{++} are very broad, making it difficult to measure the properties and differentiate between a bound state and a scattering state. For a long time, the status of the 0^{++} states as particles was debated, and with the words of Jaffe, “[they were] exiled to the gulag of particle physics“ [2]. Only in the last decade they were reintroduced as particles due to new experiments such as KLOE in the $e^-e^+ \rightarrow \pi^0\pi^0\gamma$ channel [3] or BES in the $J/\Psi \rightarrow \omega\pi^-\pi^+$ [4] channel (see [5] and the references therein for a more thorough compilation). Also recently, different data analysis approaches, utilizing the Roy-equation and derivations of it, deduce a pole mass of $m_\sigma \approx 450$ MeV for the lightest 0^{++} particle, called σ or $f_0(600)$ [6]. In light of this experimental evidence, the existence of 0^{++} as bound states can be seen as proven, but the interpretation as $(q\bar{q})$ has conceptual problems. In the following, a collection of arguments is provided that point out the main difficulties of the $(q\bar{q})$ picture. The corresponding nonet is depicted on the left side in Fig. 1.2:

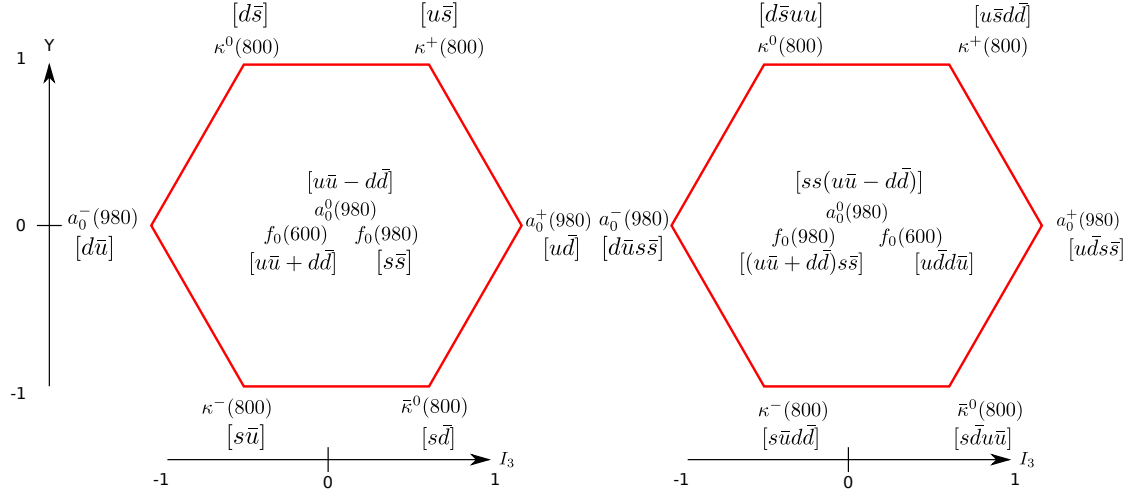


Figure 1.2: *Left:* The 0^{++} nonet in a $(q\bar{q})$ picture. *Right:* The tetraquark flavor nonet with quantum numbers 0^{++} [7]. The flavor content is denoted in brackets. A thorough and detailed review of the flavor and color content of tetraquarks can be found in [8].

1. The mass of the σ ($m_\sigma \approx 450$), the iso-scalar of the nonet, is lower than the mass of the ω ($m_\omega \approx 800$ MeV), the iso-scalar of the 1^{--} nonet. From a non-relativistic point of view, the ordering should be the reversed. In the non-relativistic quark model, charge and parity are connected with the spin (S) and the orbital momentum (L) of the two-body state: $P = (-1)^{L+1}$ and $C = (-1)^{L+S}$. This corresponds to $S = 1, L = 1$ in the 0^{++} case, and to $S = 1, L = 0$ in the 1^{--} case. As in atomic physics, states with higher angular momentum should have higher masses. This hierarchy seems clearly violated for the $(q\bar{q})$ picture. Additionally, results from lattice calculations [9] indicate that the a_0 states in the $(q\bar{q})$ scalar nonet reside well above 1 GeV, underlining that the lowest-lying (0^{++}) nonet is not a two-body state.
2. The $f_0(980)$ decays mainly to $\pi\pi$ and KK , the dominating decay channel of $a_0(980)$ is $\eta\pi$ and KK [10]. Both decays are difficult to explain by the quark content of a $(q\bar{q})$ nonet, considering that a_0 and f_0 do not possess strange quarks. For simplicity, the scalar nonet is assumed to be a state that exhibits ideal mixing. This means that $f_0(980)$ and $f_0(600)$ can be described by their strangeness and results in $f_0(980)$ containing no strange quarks. Even if abandoning the ideal mixing, which would explain the decay channel of $f_0(980)$ into KK , the oddity of the a_0 decay channels remain. Similarly, the dominating decay of $f_0(600)$ into $\pi\pi$ is not reflected by its quark content.

-
3. The 0^{++} states are much broader than the $(q\bar{q})$ states of other nonets in the same mass-region, for example the 0^{-+} . This seems odd, because the decay of mesons via quark-antiquark annihilation diagrams is governed by the Okubo-Zweig-Iizuka rule (OZI) [11, 12, 13]. Because of the similar quark content, similar decay channels and similar widths are expected, which is apparently not the case.
 4. The overall mass spectrum of the 0^{++} nonet does not reflect the quark content. As exhibited in the 0^{-+} nonet, the lowest-lying states should be the iso-triplet and the highest lying state the iso-scalar. This is clearly reversed for the 0^{++} nonet in a $(q\bar{q})$ picture.

As remedy for this unexpected behavior of the 0^{++} nonet, Jaffe [7] proposed in the 70's a different model, namely the tetraquark model with $(qq\bar{q}\bar{q})$ quark content. The advantages of the tetraquark model as explanation for the scalar nonet are striking.

The decomposition of the tetraquark tensor product $(3 \otimes 3 \otimes \bar{3} \otimes \bar{3})$ contains, besides other structures, a flavor nonet. So the tetraquark picture is in principle suitable to describe the scalar sector. The tetraquark nonet is depicted in Fig. 1.2. All the difficulties with the $(q\bar{q})$ picture disappear and the observed oddities are naturally explained by the flavor structure of the $(qq\bar{q}\bar{q})$ nonet:

1. It can be shown that in the 0^{++} case, the orbital angular momentum of a tetraquark is zero [8]. This is conform with the expectation that S-wave states should be the lightest states.
2. . The decay channels can directly be linked with the flavor content of the tetraquark. The decay of a_0 and f_0 into KK and $\eta\pi$ is caused by the strange quark content. Also, the dominant decay channel $f_0(600) \rightarrow \pi\pi$ is explained by the absence of strange quarks.
3. The broadness of the 0^{++} states can be explained by a decay into two mesons. Because these decay diagrams do not contain gluon lines, the channels are 'OZI-super-allowed' [7]. On the other hand, the decay channels of $(q\bar{q})$ states contain gluon lines and therefore are expected to be more narrow.
4. The mass spectrum deduced from the tetraquark nonet is inverted upon comparison with the spectra of the $(q\bar{q})$ nonet. The iso-scalar particle, the $f_0(600)$, is expected to have a lower mass than the iso-vector particles a_0 , because the iso-scalar does not contain any strange quark. This is exactly the structure that is found experimentally.

Apart from these phenomenological arguments, based on the group structure of the tetraquark flavor nonet, there exist lattice calculations that back up the tetraquark picture

for the lowest 0^{++} nonet [14, 15, 16].

In this thesis, the tetraquark is approached from a different perspective. A combined covariant and non-perturbative Dyson-Schwinger/Bethe-Salpeter approach in and beyond the rainbow-ladder truncation has been proven to describe various hadron observables quite well, see [17, 18] for reviews of the field. Especially the properties of the light mesons as the π, ρ [19], but also the nucleon and the Δ resonance [20, 21] are well described by this approach.

In the case of baryons, it proved viable to reduce the three-body to a two-body problem by replacement of two quarks with an effective diquark [22]. This successful application of the diquark-quark picture for the nucleon suggests to apply a similar approach to the tetraquark case. In order to reduce the four-body problem, the division into two sets of effective degrees of freedom seems natural. One combines $(q\bar{q})$ to two effective mesons (pions), the other one employs a $(\bar{q}\bar{q})$ and (qq) arrangement. As seen in chapter 4, this corresponds to a coupled meson-meson/antidiquark-diquark picture. This approach is subsequently used to calculate the mass of the $f_0(600)$.

The structure of the thesis is as follows: In chapter 2 a brief overview of the building blocks of Quantum chromodynamics (QCD) is given as well as Dyson-Schwinger equations (DSE), which are an important tool to describe QCD in an inherent non-perturbative way. Chapter 3 describes the solution of the quark DSE and the homogeneous Bethe-Salpeter equation (BSE) for pseudo-scalar mesons and scalar diquarks.

In chapter 4 the tetraquark BSE is introduced and subsequently reduced to a two-body equation employing a meson-meson/antidiquark-diquark picture. Numerical details are given in chapter 5 and the results are presented and discussed in chapter 6.

2 Quantum chromodynamics and Dyson–Schwinger equations

QCD describes the dynamics of quark fields $\Psi(x_\mu)$, $\bar{\Psi}(x_\mu)$ and gluon fields $A_\mu^a(x_\mu)$, the up to now fundamental particles of the strong interaction sector of the standard model. The corresponding action reads

$$S_{QCD}[A_\mu^a, \Psi, \bar{\Psi}] = \int d^4x \mathcal{L}_{QCD} = \int d^4x \left[\bar{\Psi}(\not{D} + m)\Psi + \frac{1}{4} F^{a,\mu\nu} F_{a,\mu\nu} \right] \quad (2.0.1)$$

where the covariant derivative is

$$\not{D} = \gamma_\mu D^\mu = \gamma_\mu (\partial^\mu + ig A^{a,\mu} T^a), \quad (2.0.2)$$

and the field-strength tensor reads

$$F^{a,\mu\nu} = \partial^\mu A^\nu - \partial^\nu A^\mu - ig [A^{a,\nu}, A^{a,\mu}]. \quad (2.0.3)$$

As usual, Greek letters denote Lorentz indices and Latin letters the color index. To simplify the notation the indices and explicit functional dependencies are omitted whenever the nature of the quantity is obvious and can be deduced from the context. The underlying continuous symmetry operation of QCD reads

$$\Psi(x) \rightarrow U(x)\Psi(x) := \exp(-ig\epsilon(x)^a T^a). \quad (2.0.4)$$

The bare coupling is denoted by g , $\epsilon(x)$ stands for the local displacement and T^a for the generators of the gauge group. Due to the lack of a suitable 'real' world analogy everything connected with the symmetry group of the strong interaction is specified by the adjective 'color'.

In the standard model the color group is $SU(3)$ and the generators form an algebra satisfying the commutator relation $[T^a, T^b] = if_{SU(3)}^{abc} T^c$. The quantities f^{abc} are the unique structure constants of $SU(3)$ and have the following values:

$$\begin{aligned}
f^{123} = 1, \quad f^{147} = f^{165} = f^{246} = f^{257} = f^{345} = f^{376} = \frac{1}{2}, \\
f^{458} = f^{678} = \frac{\sqrt{3}}{2}.
\end{aligned} \tag{2.0.5}$$

One possible fundamental representation of the eight generators are the so-called Gell-Mann matrices $\lambda^a = 2T^a$ [23]. In order to ensure local gauge invariance of the Lagrangian, the involved operators have to obey the transformation rules

$$D_\mu \rightarrow UD_\mu U^\dagger, \quad F_{\mu\nu} \rightarrow UF_{\mu\nu}U^\dagger, \quad A_\mu \rightarrow UA_\mu U^\dagger + \frac{i}{g}A_\mu U \partial_\mu U^\dagger. \tag{2.0.6}$$

The term 'local' refers to the x -dependence of the group operator $U(x)$. Because of the the non-commutativity of the group generators, which manifests itself in the commutator term in Eq. (2.0.3), QCD is called non-Abelian. That innocent-looking term encodes cubic and quartic self interactions of the gauge field which causes the coupling strength to increase with lower energies. As a consequence perturbation theory becomes non-applicable for phenomena, prevalent in the low-energy regime such as confinement and the formation of bound states.

Having the Lagrangian at hand, the generating functional of the theory in Euclidean space time can be defined as

$$\begin{aligned}
Z[J, \eta, \bar{\eta}, \sigma, \bar{\sigma}] &:= \int \mathcal{D}[A, \Psi, \bar{\Psi}, c, \bar{c}] \exp \left(\int dx^4 (-S_{QCD}[A, \Psi, \bar{\Psi}] - S_{g+f}[A, c, \bar{c}] + S_{sc}) \right) \\
&:= \exp(-W[J, \dots]).
\end{aligned} \tag{2.0.7}$$

The integration measure \mathcal{D} is to be understood as an integration over all field configurations:

$$\mathcal{D}[A, \dots] \propto \prod_x dA(x) \dots \tag{2.0.8}$$

The additional contribution to the action, S_{g+f} , contains the Faddeev-Popov ghost (first and second term) and the gauge fixing term [24]

$$S_{g+f}[A, c, \bar{c}] := \partial^\mu \bar{c}^a \partial_\mu c^a + g f^{abc} A_\mu^c \partial^\mu \bar{c}^a c^b + \frac{1}{2\xi} \partial^\mu A_\mu^a \partial^\nu A_\nu^a. \tag{2.0.9}$$

S_{sc} represents the artificial external source terms of the corresponding field and is used in the calculation of the Green functions

$$S_{sc} = A_\mu^a J_\mu^a + \bar{\eta}\Psi + \bar{\Psi}\eta + \bar{\sigma}c + \bar{c}\sigma. \quad (2.0.10)$$

In this framework the choice of ξ defines the gauge. Setting ($\xi = 1$) is called Feynman gauge and another common choice, ($\xi = 0$), is referred to as Landau gauge. This is also the choice for this work. All in all, the physical content should be independent of the value of ξ .

The ghost fields c, \bar{c} and the corresponding sources are Grassmann valued functions. Upon performing the derivation of the (perturbative) inverse gluon propagator, it turns out that the eigenvalue spectrum contains a zero rendering the inversion impossible without further constraints. Different than in Abelian theories a simple exclusion of the longitudinal component (Gupta-Bleuler formalism) is not viable due to the covariant derivative containing the gauge field itself. One way to exclude the unphysical states consistently are the above mentioned Faddeev-Popov ghost fields. This artificially fields arise if the dependence of the gauge condition G_a on the gauge fields is correctly treated. Doing this surmounts in an additional factor to the generating functional Z , written in the first line [25]:

$$\int \mathcal{D}[\omega, \epsilon] \exp\left(\frac{1}{2\xi} \int dx^4 \omega(x)^a \omega(x)^a\right) \delta(G^a(\epsilon^a)) \det\left(\frac{\delta G^a}{\delta \epsilon^b}\right) \quad (2.0.11)$$

$$G^a := \partial^\mu A_\mu^a - \omega^a \quad (2.0.12)$$

$$\det\left(\frac{\delta G^a}{\delta \epsilon^b}\right) := -\partial^\mu (\delta_\mu^{ab} + g f^{abc} A_\mu^c). \quad (2.0.13)$$

As before ϵ is the gauge group transformation. The function ω is an auxiliary quantity. Rewriting the determinant as a Gaussian integral over Grassmann fields c, \bar{c} and performing the integral over ω yields the Faddeev-Popov and the gauge fixing terms in Eq. (2.0.9).

To obtain physical observables the time ordered vacuum expectation values (VEV) of the relevant products of fields have to be calculated. With the generating functional at hand, this can be achieved by taking functional derivatives with respect to the sources and afterwards setting these sources to zero similar to the calculation of expectation values in statistical physics. To simplify the notation, the product of n timeordered fields is written as $G_n[\phi]$ (Green function) with ϕ encoding the appropriate number and type of the fields and T the timeordering operator. All sources are expressed by J , and S

contains all terms of the action defined above. The corresponding VEV of the Green function reads:

$$\langle 0|T(\phi_1 \dots \phi_n)|\rangle := \langle 0|G_n[\phi]|0\rangle = \frac{\int \mathcal{D}[\phi] \exp(-S[\phi]) G_n[\phi]}{\int \mathcal{D} \exp(-S[\phi])} \propto \frac{\delta^n}{\delta J^n} \Bigg|_{J=0} Z[J]. \quad (2.0.14)$$

To obtain the connected Green functions \hat{G}_n , instead of $Z[J]$ the (Schwinger) functional $W[J] = -\ln Z[J]$ is used. This functional can be related to the quantum effective action $\Gamma[\Phi_J]$ via a Legendre transformation

$$W[J] = \Gamma[\Phi_J] + \int d^4x J(x) \Phi_J(x) \quad (2.0.15)$$

$$\Phi_J := Z[J]^{-1} \int \mathcal{D}[\phi] G_n[\phi] \exp\left(-S[\phi] + \int d^4x J\phi\right) = \frac{\delta}{\delta J} W[J]. \quad (2.0.16)$$

It is important to note that Φ_J is not the field previously called ϕ but the field averaged with the altered action due to the Legendre transform in presence of a source. With the quantum action at hand, the 2-point Green function, the inverse propagator, can be calculated by differentiating the quantum action with respect to the averaged fields instead of differentiating the generating functional $W[J]$ with respect to the sources [26]:

$$\Delta^{-1} = \frac{\delta^2 W[J]}{\delta J \delta J} \Bigg|_{J=0} = \left(\frac{\delta^2 \Gamma[\Phi]}{\delta \Phi \delta \Phi} \Bigg|_{\Phi=\Phi_0} \right)^{-1}. \quad (2.0.17)$$

Φ_0 is the (VEV) of the field without external sources. Higher order one particle irreducible (1PI) vertices can be calculated by subsequently taking functional derivatives of the quantum effective action. The Dyson-Schwinger equations (DSE) [27, 28] can be derived by stating that the generating functional $Z[J]$ should be invariant to translation operation on the involved fields ϕ . Following the derivation in [29] that applies a superfield formalism that essentially hides the involved fields behind Φ_i , a variation of the functional $Z[J]$ yields:

$$\begin{aligned} 0 &= \frac{\delta}{\delta \phi_i} Z[J] = \int \mathcal{D}[\phi] \left(-\frac{\delta S}{\delta \phi_i} + J_i \right) \exp\left(-S + \int \phi_j J_j\right) = \\ &= \left(-\frac{\delta S}{\delta \phi_i} \Bigg|_{\phi=\delta/\delta J_i} + \frac{\delta \Gamma[\Phi]}{\delta \Phi_i} \right) \exp(W[J]). \end{aligned} \quad (2.0.18)$$

Upon further manipulations the generating DSE can be deduced:

$$\frac{\delta\Gamma[\Phi]}{\delta\Phi_i} = \left. \frac{\delta S}{\delta\phi_i} \right|_{\phi=\Phi_i+\Delta_{ij}^J\delta/\delta\Phi_j}. \quad (2.0.19)$$

Δ_{ij}^J denotes the, due to the super field formalism possible mixed, propagator in presence of a source. Sequentially differentiating the left side gives the various vertex functions and propagators of the theory. An automated *Mathematica* based program to calculate DSE for arbitrary actions can also be found in [29].

The resulting DSEs for the propagators and various vertices have the beauty to describe the whole picture including all perturbative and non perturbative contributions. A caveat is the fact that the DSEs are all dependent on each other thus forming an infinite non linear system of equations. This renders an exact solution of the Green functions numerically impossible. To resolve some of the non perturbative properties, for example the dynamical chiral symmetry breaking (D_χ SB) of the quark, and still being able to solve the DSE in a tractable time, a suitable truncation of the system of equations has to be applied.

2.1 Quark DSE

By differentiating Eq. (2.0.19) with respect to a quark field, the quark propagator can be extracted which reads in a diagrammatic notation:

$$\text{Diagrammatic equation (2.1.1)} \quad (2.1.1)$$

The blobs indicate that the involved quantities are dressed containing the full set of all possible quantum effects. The wiggly lines represent the gluon, the straight line a quark and the blue blob the full quark-gluon vertex which all themselves satisfy their own DSE. The involved functions (in Euclidean space) depend on the renormalization scale μ . The gluon propagator in Landau gauge ($\xi = 0$) reads

$$D_{ab}^{\mu\nu}(k, \mu) = \delta^{ab} \left(\frac{\mathcal{G}(k^2, \mu)}{k^2} \left(\delta^{\mu\nu} - \frac{k^\mu k^\nu}{k^2} \right) + \xi \frac{k^\mu k^\nu}{k^4} \right). \quad (2.1.2)$$

$\mathcal{G}(k^2, \mu)$ is the renormalization point dependent dressing function and the δ -function acts in color space. The part in brackets can be regarded as the transverse projector $T^{\mu\nu}(k)$ effectively killing the k^μ longitudinal part of the quark gluon vertex. The left vertex is bare by default:

$$(\Gamma_{bare})_{abc}^\mu = g Z_{1F} i \gamma^\mu T_{ab}^c. \quad (2.1.3)$$

Z_{1F} denotes the multiplicative vertex renormalization constant and T_{ab}^c the color generators. The second quark-vertex is dressed and consists of twelve elements. The number and structure of these elements is derived by the tensor product $\{\gamma^\mu, k^\mu, l^\mu\} \otimes \{\mathbb{1}, \not{k}, \not{l}, [\not{k}, \not{l}]\}$ with $l^\mu = p^\mu - k^\mu$. The dressed vertex in rainbow-ladder truncation on the right side of the DSE reads

$$\Gamma^\mu(l, k, \mu)_{abc} := g i \gamma^\mu f_1(k^2, \mu) T_{ab}^c. \quad (2.1.4)$$

In this truncation only the dressing function f_1 , corresponding to the $\gamma^\mu \mathbb{1}$ structure, is retained. A discussion of the quark-gluon vertex in rainbow-ladder truncation, using all twelve different tensor structures, can be found in [30]. The bare (inverse) quark propagator outside the loop integral reads

$$S_{bare}^{-1}(p, \mu) = \delta^{ab} Z_2(\mu, \Lambda) (i \not{p} + m_0(\Lambda)) \quad (2.1.5)$$

and the dressed one

$$S(p, \mu) = \delta^{ab} \frac{Z_f(p^2, \mu) (-i \not{p} + M(p^2))}{p^2 + M^2(p^2)} := (\mathbb{1} \sigma_{sc}(p^2, \mu) - i \not{p} \sigma_{vc}(p^2, \mu)) \delta^{ab}. \quad (2.1.6)$$

$M(p^2)$ is the momentum-dependent quark-mass function and $Z_f(p^2, \mu)$ the quark dressing function. The functions σ_{sc} and σ_{vc} on the far right side are called the scalar and vector dressing functions, respectively. The bare mass $m_0(\Lambda)$ depends on the regularization cutoff Λ and can also be written as

$$m_0(\Lambda) = m_\mu Z_m(\Lambda, \mu). \quad (2.1.7)$$

The cutoff and renormalization scale dependent Z_m is the so-called mass renormalization constant. Using a result from perturbative QCD [25]

$$m_\mu = m_\nu \left(\frac{\ln(\nu^2/\Lambda_{QCD}^2)}{\ln(\mu^2/\Lambda_{QCD}^2)} \right)^{\gamma_m}, \quad (2.1.8)$$

m_μ can be calculated from m_ν , the experimental measured current quark mass at an energy scale which is typical in the order of 2 GeV. The numerical values for the scale parameter Λ_{QCD} , the anomalous dimension γ_m and the mass m_μ are given in the next section. For a sufficiently high enough renormalization point μ , the values for $M(\mu)$ and m_μ are identical [31] which is the case for $\mu = 19$ GeV, the value chosen throughout this work. The equality $M(\mu) = m_\mu$ provides a tool to deduce the value for $m_0(\Lambda)$ in a self-consistent way.

Applying a Slavnov-Taylor identity (STI) $Z_{1F} = Z_2/\tilde{Z}_3$ [32] with \tilde{Z}_3 as the ghost renormalization constant, and subsequently collecting the gluon dressing and the vertex dressing into one quantity yields:

$$\alpha(k^2, \mu) := \frac{g^2}{4\pi Z_2 Z_3} \mathcal{G}(k^2, \mu) f_1(k^2, \mu). \quad (2.1.9)$$

The dressing function together with the bare gluon propagator forms the effective gluon of the model. The corresponding quark DSE reads

$$\begin{aligned} \frac{1}{Z_f(p^2)} (i\not{p} + M(p^2)) &= Z_2(i\not{p} + m_0) \\ &+ c_{col} \frac{4\pi}{(2\pi)^4} Z_2^2 \int d^4q \gamma^\mu \frac{Z_f(q^2)(-i\not{q} + M(q^2))}{q^2 + M^2(q^2)} \gamma^\nu \frac{\alpha(k^2) T^{\nu\mu}(k)}{k^2}. \end{aligned} \quad (2.1.10)$$

with the relation $:= p - q$. The dependence on the renormalization/regularization parameters is suppressed. Carrying out the implicit color trace inside the loop integral yields a factor of $c_{col} = \frac{4}{3}$.

2.2 Effective gluon

In this work, the effective interaction $\alpha(k^2)$ that combines the gluon and quark-gluon vertex dressings is modeled by the Maris-Tandy interaction [33, 19]

$$\alpha(k^2) = \frac{c\pi}{\omega^7} \left(\frac{k^2}{\Lambda_0^2} \right)^2 \exp(-k^2/(\omega^2\Lambda_0^2)) + \frac{\pi\gamma_m (1 - \exp(-k^2/\Lambda_0^2))}{\ln \sqrt{e^2 - 1 + \left(1 + k^2/\Lambda_{QCD}^2\right)^2}}. \quad (2.2.1)$$

$\Lambda_{QCD} = 0.234$ GeV and $\Lambda_0 = 1$ GeV are scale parameters. $\gamma_m = \frac{12}{25}$ is the anomalous dimension of the quark propagator for $N_{c(olor)} = 3$ and $N_{f(lavour)} = 4$. The parameters

c and ω are chosen throughout this work as $c = 0.37$ and $\omega = 0.4$. The mass at the renormalization point $\mu = 19$ GeV is set to $m_\mu = 0.0037$ GeV for both u and d quarks assuming that isospin is a good symmetry of QCD. This set of parameters reproduces the decay constant of the pion $f_\pi = 131$ MeV at a pion mass $m_{pi} = 138$ MeV [33].

The two parts of the effective interaction correspond to two structural considerations: The second part encodes the correct behavior of the quark-gluon coupling of perturbative QCD in the UV-regime and the first part ensures a sufficient enhancement in the near-infrared which leads to dynamical chiral symmetry breaking for the quark.

In order to collect all relevant parameters in one spot, the values for the ultraviolet (UV) and infrared (IR) cutoff used in the DSE and BSE are also given: $\Lambda_{UV}^2 = 10^6$ GeV and $\Lambda_{IR}^2 = 10^{-9}$ GeV.

2.3 Solving the quark DSE

With an ansatz for $\alpha(p^2)$ at hand, the DSE can be solved in a self-consistent manner. The unknown functions and values in this equation are the dressing functions $M(p^2)$ and $Z_f(p^2)$, the renormalization constant Z_2 and the cutoff dependent mass m_0 . Starting with Eq. (2.1.10) the scalar part of the quark can be projected out via tracing in the Dirac space yielding the mass function $M(p^2)$. The vector part can be extracted by multiplication with \not{p} and subsequently taking the trace in the Dirac space.

The mass m_0 and Z_2 can be directly extracted from the evaluation of the DSE at the renormalization point μ with the renormalization condition $Z_f(\mu^2) = 1$ and $M(\mu^2) = m_\mu$. The resulting system of equations has the form:

$$\begin{aligned} M(p^2) &= Z_2 F(p^2) m_0 + Z_2^2 Z_f(p^2) \frac{4}{3\pi^2} \int dq d\theta \frac{\alpha(k^2) M(q^2) Z_f(q^2) q^3 \sin^2(\theta)}{(q^2 + M^2(q^2)) (p^2 + q^2 - 2pq \cos(\theta))} \\ &= Z_2 Z_f(p^2) m_0 + Z_2^2 \text{Int}_M \end{aligned} \quad (2.3.1)$$

$$\begin{aligned} \frac{1}{Z_f(p^2)} &= Z_2 + Z_2^2 \frac{4}{3\pi^2 p^2} \int dq d\theta \alpha(k^2) Z_f(q^2) q^3 \sin^2(\theta) \times \\ &\quad \frac{3 \cos(\theta) (pq^3 + qp^3) - 4p^2 q^2 \cos^2(\theta) - 2p^2 q^2}{(q^2 + M^2(q^2)) (p^2 + q^2 - 2pq \cos(\theta))^2} \\ &= Z_2 + Z_2^2 \text{Int}_F \end{aligned} \quad (2.3.2)$$

$$m_0 = \frac{M(\mu^2) - Z_2^2 \text{Int}_M(\mu)}{Z_2} \quad (2.3.3)$$

$$Z_2 = \frac{\sqrt{1 + 4 \text{Int}_F(\mu)} - 1}{2 \text{Int}_F(\mu)}. \quad (2.3.4)$$

The fundamental obstacle to overcome in solving this integral equation is the dependence of the integral on the unknown functions M and Z_f . To solve this self-consistent problem, a suitable representation of the functions that allows to evaluate them at arbitrary points inside the integral is necessary ensuring that any integration method can be used.

A tractable way to represent a function is an expansion in Chebyshev polynomials of the 1. kind. They have the property to have the smallest maximum of all interpolating polynomials of a given order (MinMax polynomials). This makes them less sensitive to Runge's phenomenon, an effect that describes the behavior of high order interpolation polynomials on an equidistant grid to exhibit erratic oscillations with high amplitudes. The Chebyshev polynomials are thus not defined on an equidistant grid but on the Chebyshev nodes

$$x_j = \cos(\pi(j - 0.5)/N). \quad (2.3.5)$$

The parameter N gives the order of the maximal Chebyshev polynomial used in the expansion. An algorithm (Clenshaw-Curtis) featuring a fast way to calculate the approximated function at an arbitrary value can be found in [34].

With this expansion at hand the procedure to solve the coupled equation is straightforward: Starting with an initial guess for Z_2 , m_0 and the functions $M(p^2)$ and $Z_f(p^2)$ at the Chebyshev nodes, the right-hand side of Eq. (2.3.1) and (2.3.2) is calculated using a standard Gauss-Legendre method. This in turn gives a new guess for the sought-after functions and is repeated until $\sum_j |M(p^2)| \leq \epsilon$ and $\sum_j |Z_f(p^2)| \leq \epsilon$ for some ϵ at the order of 10^{-6} . The renormalization constant Z_2 and the bare mass m_0 are also calculated at every iteration step.

As this technique will be used in the following investigations, a few remarks on the details are pending. Instead of integrating over p directly, a transformation to a logarithmic grid is advisable. This takes into account the wide range of the interval $[0, \Lambda_{UV}]$ that p lies in.

The drawback of a logarithmic grid is the introduction of an infrared cutoff because the interval $[0, \Lambda_{UV}]$ is transformed to $[-\infty, \log(\Lambda_{UV})]$. In practice though, this is not a problem because the Gauss-Legendre algorithm does not evaluate the end points. Thus, an exclusion of $p = 0$ introduces only a minor error, especially taking into account the smallness of the infrared cutoff.

Instead of the function $M(p^2)$ itself, the exponent was expanded in a Chebyshev polynomial which effectively results in taking the logarithm of the first line in Eq. (2.3.1). The reason behind this step is the idea that the exponent of a function that spans several magnitudes, which is the case for $M(p^2)$, is smoother than the function itself. An

approximation of the only slightly varying exponent is more accurate and improves the approximant overall.

A caveat to this procedure is the sign problem. For as long as one can assure that the sign of the function does not change in the integration interval, an approximation of the exponent is applicable. In the present case, the quark dressing functions of the Maris-Tandy model are well known [17] and the procedure is legitimate. Another technical detail regarding the integration process is the division of the integration interval into smaller parts and using a Gauss-Legendre integration on each section separately. The division points were chosen to be the Chebyshev nodes. To be able to do this, an evaluation at arbitrary integration values is the key feature and underlines the advantage of the Chebyshev expansion. Keeping in mind that at every integration point on the p -axis another integration over the angular variable θ is included, the calculation time was reduced to less than a minute by a parallel evaluation of the integral using the framework of *OpenMP* for C++ [35]. The gain in computation time is not of great importance for quark DSE, which is fast to solve anyway, but turned out to be invaluable in the calculation of the tetraquark BSE.

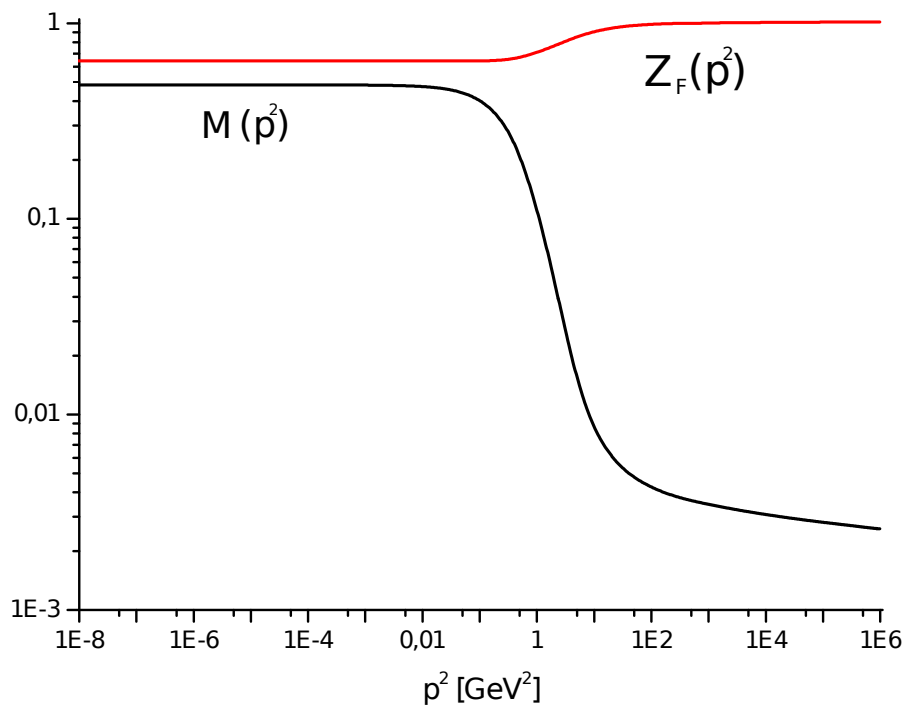


Figure 2.1: Self-consistent solution of the quark DSE. The renormalization constant was calculated to $Z_2 = 0.982301$ and $m_0 = 0.00251906$ GeV.

The general feature of D_χ SB in the quark propagator can be seen in fig. 2.1. The mass

function $M(p^2)$ acquires a substantial enhancement in the infrared region, with the onset of a rapid decay around 0.3 GeV, thus setting the scale of (non-perturbative) QCD. A similar behavior at the same momentum regime can be seen in the quark dressing function $Z_f(p^2)$. For higher momenta, the dressing function $Z_f(p^2)$ approaches Z_2 , whereas the mass function exhibits a logarithmically decaying tail.

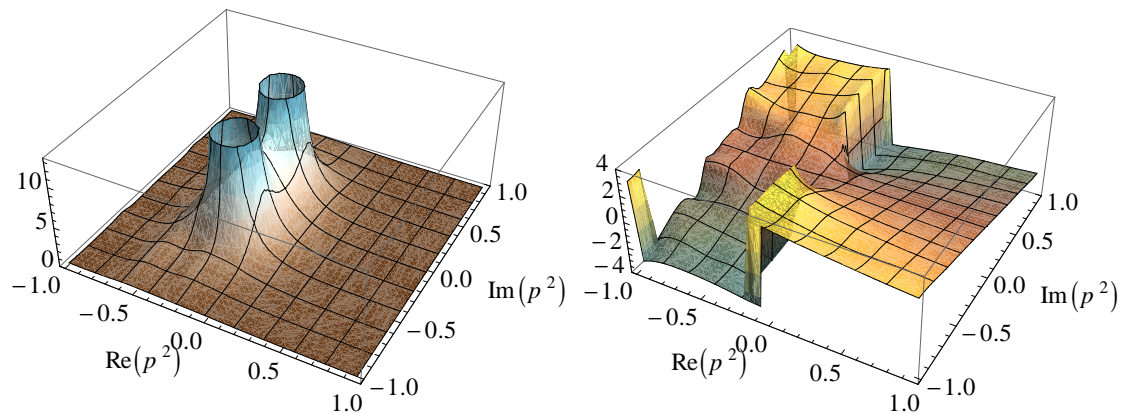


Figure 2.2: *Left:* The absolute value of the quark propagator’s vector dressing function σ_{vc} with complex conjugated poles in the complex plane. *Right:* The argument of the vector dressing function. The cut structure, visible by the discontinuity in the argument, can be traced back to the logarithmic function in the effective coupling, Eq. (2.2.1).

2.4 Solving the quark DSE for complex momenta

The DSE solution obtained so far determines the dressing functions only for real and positive momenta inside the integration boundaries. In the meson and tetraquark BSEs though, the momenta are of the form

$$p^2 = (q + \eta P)^2 = q^2 + \eta^2 P^2 + 2\eta z \sqrt{q} \sqrt{P}, \quad z = \frac{q \cdot P}{\sqrt{q^2} \sqrt{P^2}}. \quad (2.4.1)$$

Whenever $P^2 \leq 0$ holds, the momenta are shifted towards the negative real axis and into the complex plane.

The variable η specifies the momentum sharing parameter. Throughout this work, the sharing parameter is chosen to be $\eta = \frac{1}{2}$. This reflects the equal mass symmetry of the quarks and mesons/diquarks in the meson and tetraquark BSE. Since the approach is fully covariant, the observables are independent of the momentum sharing parameter [36].

The singularity structure of the quark propagator in rainbow-ladder truncation turns out to be given by complex-conjugated poles. This feature of the quark DSE is preserved in more general studies [30, 37] and puts a constraint on the kinematical region that is usable in the meson and tetraquark BSEs. In the case of the meson BSE, the integration interval lies in the interior of the parabola $(p \pm i\frac{1}{2}M)^2$. Upon comparison of the interior of the parabola with the pole positions of the quark and meson propagators, the constraints on the bound-state mass of the meson (M_2) and the tetraquark (M_4) are

$$M_2 \leq 2m_q, \quad M_4 \leq 2m_\pi. \quad (2.4.2)$$

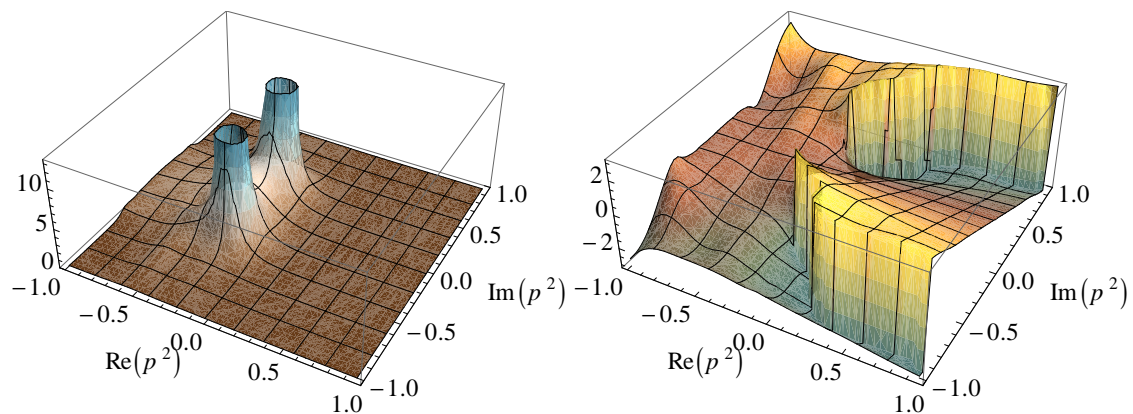


Figure 2.3: *Left:* The absolute value of the quark propagator’s scalar dressing function σ_{sc} with complex conjugated poles in the complex plane. *Right:* The argument of the scalar dressing function. The cut structure, visible by the discontinuity in the argument, can be traced back to the logarithmic function in the effective coupling, Eq. (2.2.1).

The relation for the tetraquarks follows from the constraint of the meson propagator and the meson mass. Without a procedure to take the explicit residues into account, this restricts the bound mass in the meson BSE to values 1 GeV which is well above the masses for the lowest pion and diquark states [38]. In the case of the diquark-diquark/meson-meson BSE, the restriction is harsher and puts the value for $\sqrt{P^2}$ below $2m_\pi \approx 280$ MeV.

Sophisticated methods to solve the quark propagator in the complex plane exist [39, 40, 21]. The basic principle is a change in the momentum routing of the quark DSE. For instance, the quark loop momentum q in Eq. (2.1.1) can be shifted and the problem can be solved on a contour in the complex plane featuring the form of a parabola defined by Eq. (2.4.1). Applying Cauchy’s theorem, the dressing function can be evaluated for

arbitrary points inside the contour.

However, the specific infrared behavior of the effective coupling in Eq. (2.2.1) that contains functions that allow a complex continuation, permits a simple solution method. Here the solution of the DSE on the positive real line is put into the quark DSE again, and one more iteration in Eq. (2.3.4) is performed with the external momentum set to the complex value. With the momentum routing in Fig. (2.1.1), only the gluon, known from Eq. (2.1.2) and Eq. (2.2.1), is evaluated for complex values. The singularities in the coupling induced by the logarithmic part in Eq. (2.2.1) are concealed by the large oscillating contributions of the exponential function [38].

Solving the quark DSE for complex momenta is numerically not demanding. Nevertheless a simultaneous DSE solution during the integration of the meson and tetraquark BSE is out of question because it still involves the solution of two-dimensional integrals. To speed up the evaluation, the real and imaginary parts of the quark dressing functions were precomputed on a logarithmic grid in the complex plane and a spline interpolation was used to subsequently obtain the values. Similar to the strategy used in the solution of the quark DSE, the exponents instead of the functions were stored.

The scalar and vector dressing function are plotted in Figs. 2.3 and 2.2, respectively. The complex-conjugated poles emerge for $Re(p^2) \leq 0$. The arguments of the dressing functions exhibit a discontinuity which is equivalent to branch cuts in the dressing functions. These cuts could be artifacts of the logarithmic function in the effective gluon in Eq. (2.2.1). These structures are well outside the integration domain of the meson BSE and thus have no influence on the solution.

3 Mesons and diquarks

Because the tetraquark BSE in the meson-meson/antiquark-diquark picture contains explicitly offshell meson and diquark amplitudes, a proper description of these amplitudes is necessary. In this chapter a calculation of the onshell meson and diquark amplitudes is presented and an appropriate continuation into the offshell region is provided.

3.1 Two-body equation

The homogeneous Bethe-Salpeter equation (BSE) [41] describes the bound state of two particles. In the quark-antiquark case the bound state corresponds to the (pseudo-scalar) meson and in the quark-quark case to the (scalar) diquark. The starting point is the general equation for the 4-point Green function $G = G_0 + G_0 K^{(2)} G$

$$\begin{array}{c} \text{---} \\ | \text{G} | \\ \text{---} \end{array} = \begin{array}{c} \text{---} \\ | \text{---} | \\ \text{---} \end{array} + \begin{array}{c} \text{---} \\ | \text{K} | \\ \text{---} \end{array} \begin{array}{c} \text{---} \\ | \text{G} | \\ \text{---} \end{array}, \quad (3.1.1)$$

where G_0 denotes two dressed propagators and K a suitable scattering kernel. On the mass pole M_B , the Green function separates into two contributions:

$$\begin{array}{c} \text{---} \\ | \text{G} | \\ \text{---} \end{array} = \frac{\begin{array}{c} \text{---} \\ | \Psi \Psi | \\ \text{---} \end{array}}{P^2 - M_B^2} + \text{regular parts}. \quad (3.1.2)$$

The resulting poles on both sides can be equated, yielding the homogeneous BSE for the two-body bound state amplitude Ψ

$$\begin{array}{c} \text{---} \\ | \Psi \leftarrow | \\ \text{---} \end{array} = \begin{array}{c} \text{---} \\ | \text{K} | \\ \text{---} \end{array} \begin{array}{c} \text{---} \\ | \Psi \leftarrow | \\ \text{---} \end{array} \text{ or } \begin{array}{c} \text{---} \\ | \Psi \leftarrow | \\ \text{---} \end{array} = \begin{array}{c} \text{---} \\ | \Psi \leftarrow | \\ \text{---} \end{array} \begin{array}{c} \text{---} \\ | \text{K} | \\ \text{---} \end{array}. \quad (3.1.3)$$

A detailed derivation of the BSE in ladder truncation can be found in [42]. Chiral symmetry implies that the kernel in Eq. (3.1.3) has to obey the axial vector Ward-Takahashi identity (AV-WTI) [43]:

$$\gamma_5 \Sigma(-p_-) + \Sigma(p_+) \gamma_5 = - \int K(p, q, P) (\gamma_5 S(-q_-) + S(q_+) \gamma_5), \quad (3.1.4)$$

$$(3.1.5)$$

Here, the crossed circles represent γ_5 matrices, P is the total momentum of the bound state amplitude, and the relation for the momenta reads $p_+ = p + \eta P$ and $p_- = -p + (1 - \eta)P$.

The AV-WTI constrains the explicit form of the kernel upon knowledge of the fully dressed quark propagator. In a formalism starting from an action that consists of higher correlators than just the fields (Cornwall-Jackiw-Tomboulis action) [44], a procedure is available to derive a BSE and thus a kernel that respects the AV-WTI [45, 30]. In the case of the Maris-Tandy effective interaction, the kernel can be derived by cutting the quark self-energy loop at one of the bare vertices, resulting in an (effective) gluon-exchange kernel in the pseudo-scalar meson BSE. This setup of truncated quark DSE and BSE with the same effective gluon coupling has been extensively used in the description of light mesons, see [46] for an overview; and progress was also made for baryons [47, 38]. The kernel of the BSE then reads

$$K(p, q, P) = Z_2^2 \frac{4\pi\alpha((p-q)^2)}{(p-q)^2} \left(\frac{\lambda^i}{2}\right) \left(\frac{\lambda^i}{2}\right) (i\gamma^\mu) T^{\mu\nu} (i\gamma^\nu), \quad (3.1.6)$$

with λ^i being the Gell-Mann matrices of the SU(3) color group. The final missing ingredient to completely solve the meson BSE is a proper normalization of the BSE amplitude. Since the BSE is solved by reformulation as an eigenvalue problem, see chapter 5.1, the eigenvector, identified with the amplitude, is by construction unique only up to a normalization constant. Starting from eq. (3.1.1) the equation can be reformulated as

$$G[G_0^{-1} - K]G = G. \quad (3.1.7)$$

Upon separation into pole contributions and regular terms, see Eq. (3.1.2), the residues on both sides can be equated. Subsequently exploiting the independence of the scattering kernel K on the momentum P , the normalization condition reads [48]

$$\frac{d}{dP^2} \Big|_{P^2=-M_B^2} \left[\text{Tr} \int_q^\Lambda \bar{\Gamma}(q, K) S(q + \eta P) \Gamma(q, K) S(-q + (1 - \eta)P) \Big|_{K^2=-M^2} \right] \stackrel{!}{=} 1. \quad (3.1.8)$$

Because the amplitudes contain normalized color and flavor matrices, the trace has to be taken in Dirac space only. Due to symmetrization reasons (two quarks instead of a quark-antiquark pair), the norm integral picks up a factor $\frac{1}{2}$ when in the case of diquarks. Furthermore, the indices of the amplitudes and propagators must be brought into the right order before taking the trace. In the case of the diquark norm integral, one of the quarks has the opposite direction in comparison to the meson case, see Eq. (4.2.9). This surmounts in the replacement of the corresponding propagator $S(-q_-) \rightarrow S^T(q_-)$, see also Eq. (4.3.2). An equivalent way to normalize the BSE amplitude is given in [49]:

$$\left(\frac{d \ln(\lambda(P^2))}{dP^2} \right)^{-1} \Big|_{P^2=-M^2} \stackrel{!}{=} \text{Tr} \dots \quad (3.1.9)$$

Here, the ' \dots ' stand for the trace on the left-hand side in Eq. (3.1.8) and λ corresponds to the eigenvalue obtained from the BSE for a P^2 in the neighborhood of bound-state mass. This prescription has the advantage of being independent of the kernel, regardless of its dependence on the momentum P .

3.2 Structure of the bound-state amplitudes

In principle, the pseudo-scalar meson BSE is fully determined upon knowledge of the dressed quark propagator, the (ladder) kernel and a normalization prescription. What remains is the specification of the structure of the amplitudes. A two-body bound state amplitude of (pseudo)-scalar nature has no uncontracted Lorentz index and depends on two momenta (q, P) and thus exhibits a decomposition into the following four Dirac basis elements $\tilde{\tau}_i$ [50]:

$$\tilde{\tau}_i \in \{\mathbb{1}, \not{P}, \not{q}, [\not{P}, \not{q}]\}, \quad i \in \{1, 2, 3, 4\}. \quad (3.2.1)$$

The solution strategy for the BSE uses a projection onto this four amplitudes. Thus an orthogonal basis is highly favorable and can be constructed by using \not{q}_T instead of \not{q} . The subscript stands for the transverse projection of \not{q} with respect to \not{P} . Additional

to an orthogonalization, a normalization of the basis is also carried out for convenience. This yields the following set of basis elements:

$$\tau_i(q, P) \in \left\{ \mathbb{1}, \frac{\not{P}}{\sqrt{P^2}}, \frac{z}{z(1-z^2)} \left(\frac{\not{q}}{\sqrt{q^2}} - \frac{\not{P}P \cdot q}{P^2 \sqrt{q^2}} \right), \frac{[\not{P}, \not{q}]}{4(1-z^2)\sqrt{P^2}\sqrt{q^2}} \right\}. \quad (3.2.2)$$

The dressing functions of the basis elements are denoted as $E(q^2, P^2, z)$, $F(q^2, P^2, z)$, $G(q^2, P^2, z)$, $H(q^2, P^2, z)$ or sometimes as $f_i(q^2, P^2, z)$. The index i and the characters $\{E, F, G, H\}$ denote the dressing functions in the same order as the basis elements in Eq. (3.2.2). The angular variable z is defined by

$$z := \frac{q \cdot P}{\sqrt{q^2}\sqrt{P^2}}. \quad (3.2.3)$$

In general, the set above could be multiplied by a γ_5 matrix, effectively doubling the number of basis elements. In order to reduce the number of basis elements, the quantum numbers of the pseudo-scalar mesons, namely parity and charge conjugation, have to be taken into account.

A meson amplitude $\Gamma(q, P)$ transforms under parity transformation as follows:

$$\Gamma(q, P) = -\gamma^4 \Gamma(\tilde{q}, \tilde{P}) \gamma^4. \quad (3.2.4)$$

The minus corresponds to negative parity and the tilded momenta have their spacial coordinates reflected. By inspection it can be seen that the basis elements have a parity of $+1$. A remedy of this behavior is an attachment of an γ_5 matrix in front of the basis elements, see Eq. (3.3.1), thus reducing the number of Dirac basis elements to four (again).

The charge conjugated meson and diquark amplitudes are defined as in [38]

$$\bar{\Gamma}(q, P) := C \Gamma^T(-q, -P) C^T. \quad (3.2.5)$$

The operators $C = \gamma^4 \gamma^2$ and $C^T = -C$ denote the charge conjugation matrices. With this definition, invariance under charge conjugation is equivalent to

$$\bar{\Gamma}_M(q, P) = \Gamma_M(q, -P). \quad (3.2.6)$$

Using the charge conjugation transformation properties of the γ matrices [25], it is easily shown that the basis elements in Eq. (3.2.2) are positive under charge conjugation. This

implies that the dressing functions have to be even in powers of z .

A certain type of ladder truncated BSE shows an $O(4)$ symmetry which gives rise to the expansion of the lowest lying angular momentum state in Chebyshev polynomials of the second kind [51]. This property renders the Chebyshev polynomials a suitable basis for an expansion of the BSE amplitude's angular part, too. Usually a few Chebyshev polynomials are sufficient to obtain a good description of pseudo-scalar mesons. The benefit of the expansion method is a reduction of the numerical effort because only a discretization in q is necessary instead of a discretization in q and z . In [33] a comparison between the expansion and the discretization method is carried out and verifies the rapid conversion of the Chebyshev expansion.

The expansion in even Chebyshev polynomials is also applicable for the diquark. That can be seen from the Pauli principle: the interchange of both quarks is equivalent to a transposition of the diquark amplitude and a reflection of the relative momentum vector:

$$\Gamma_D(q, P) = -\Gamma_D^T(-q, P). \quad (3.2.7)$$

This relation can be met when using $\gamma_5 \tau_i(q, P)C$ as Dirac structure of the diquark amplitude Γ_D and implicitly assuming that the dressing functions are even in z :

$$\begin{aligned} -\Gamma^T(-q, P) &= -C^T(\gamma_5 \tilde{\tau}(-q, P))^T C C^T = -\gamma_5 \tilde{\tau}_i(q, P) C^T = \gamma_5 \tilde{\tau}_i(q, P) C \Rightarrow \\ \Gamma_D(q, P) &= -\Gamma_D^T(-q, P) \end{aligned} \quad (3.2.8)$$

Additionally, it is assumed that the combined flavor and color part is symmetric under quark exchange.

Taking the efficiency in the meson case as a guideline, the expansion in Chebyshev polynomials is also employed for the tetraquark BSE amplitude.

3.3 Meson amplitudes

Following the notation of [38], the meson amplitudes can be written as

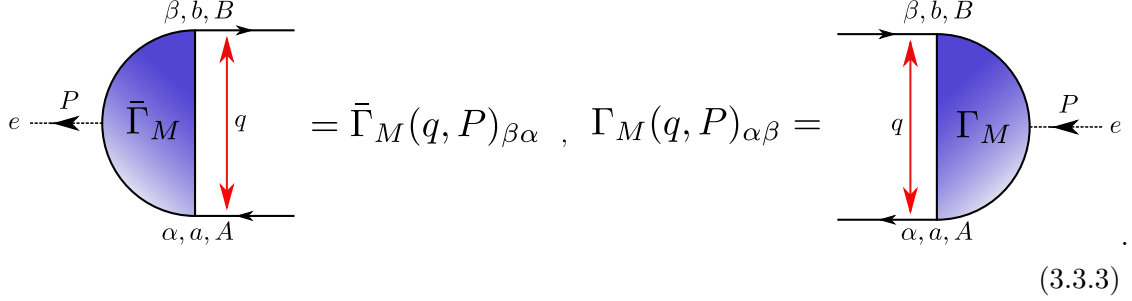
$$\Gamma_M(p, P)_{\alpha\beta} := \sum_{l=1}^4 \sum_k f(q^2, P^2) T_l(z) \{i\gamma_5 \tau_k(q, P)\}_{\alpha\beta} \otimes \frac{\delta_{AB}}{\sqrt{3}} \otimes r_{ab}^e. \quad (3.3.1)$$

The color-singlet matrix is chosen so that $\frac{\delta_{AB}\delta_{BA}}{3} = 1$ holds. The flavor matrices r

correspond to the isospin-triplet states π^+, π^-, π^0 and are given by

$$r^+ = \frac{1}{2}(\sigma_1 + i\sigma_2), \quad r^- = \frac{1}{2}(\sigma_1 - i\sigma_2), \quad r^0 = \frac{1}{\sqrt{2}}\sigma_3, \quad (3.3.2)$$

respectively, where the σ_i denote the Pauli matrices. The flavor/isospin matrices are orthogonal and normalized $Tr[\bar{r}^e r^f] = \delta_{ef}$ as well. The function $T_l(z)$ denotes the Chebyshev polynomial of the second kind.



$$(3.3.3)$$

In the pictorial representation, Greek letters denote Lorentz indices, capital Latin letters color and small ones flavor indices. The bluish colored semicircles are used to distinguish the meson amplitudes from the orange-colored diquark amplitudes. The corresponding meson BSE reads

$$\Gamma(p, P)_{\alpha\beta} = \int K(q, p, P)_{\alpha\delta, \gamma\beta} S(q_+)_{\delta\mu} \Gamma(q, P)_{\mu\nu} S(-q_-)_{\nu\gamma}. \quad (3.3.4)$$

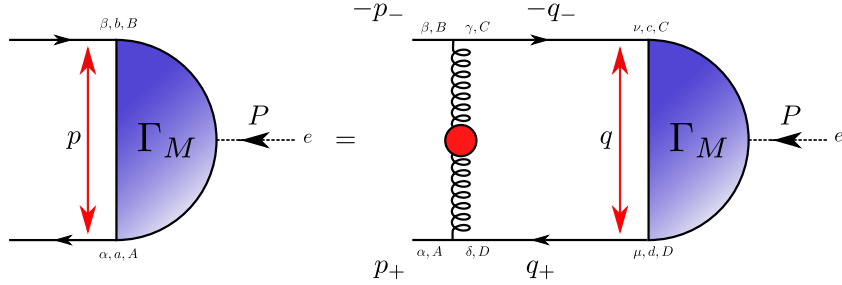


Figure 3.1: Meson BSE, see Eq. (3.3.4).

The correct momentum routing is shown in 3.1. Upon tracing the color matrices, the left-hand side yields 1 due to normalization of the amplitude and the right-hand side gives a color factor $\frac{4}{3}$ after taking into account the Gell-Mann matrices in the kernel. The flavor matrices give a trace of 1 on both sides. The flavor structure does not play a role at all because the rainbow-ladder kernel is flavor independent.

3.4 Diquark amplitudes

In section 4 it will be demonstrated that the reduction of the tetraquark bound-state equation to a two-body system requires not only mesons but also internal diquark degrees of freedom. In analogy to the description of baryons in the quark-diquark model [22, 38], the qq scattering matrix can be approximated by a sum of diquarks: This is a consequence of the rainbow-ladder truncation: despite being colored objects, diquark poles appear as an artifact of the truncation in the qq scattering matrix and vanish beyond rainbow-ladder [52]. Nevertheless, the importance of diquarks as internal binding structures in tetraquarks may persist even in a more general setup. For the present purpose a restriction to the scalar diquark only is employed.

The quantum numbers of the lowest-lying scalar diquark are $J^P = 0^+$ with the color structure of an antisymmetric color anti-triplet. The structure that fulfills this symmetry is the fully antisymmetric tensor ϵ_{ABE} , where A, B denote the colors of the quarks and E the color of the amplitude. Because of the Pauli principle, the flavor/isospin structure has to be antisymmetric, see Eq. (3.2.8). This is achieved by the antisymmetric isospin singlet matrix $s^0 = \frac{1}{\sqrt{2}}i\sigma_2$.

The replacement of the antiquark with a quark is expressed by insertion of a \mathcal{C} matrix. The amplitude can then be written as

$$\Gamma_D(p, P)_{\alpha\beta} := \sum_{l=1}^4 \sum_k f(q^2, P^2) T_l(z) \{i\gamma_5 \tau_k(q, P) \mathcal{C}\}_{\alpha\beta} \otimes \frac{\epsilon_{ABE}}{\sqrt{2}} \otimes s_{ab}^0. \quad (3.4.1)$$

As in the meson case, the isospin and color matrices are chosen to be normalized upon tracing. The corresponding rainbow-ladder BSE looks almost the same as in the meson case, except for the change of the antiquark to a quark, see Fig. 3.2.

$$\Gamma(p, P)_{\alpha\beta} = \int K(q, p, P)_{\alpha\delta, \beta\gamma} S(q_+)_{\delta\mu} \Gamma(q, P)_{\mu\nu} S^T(q_-)_{\nu\gamma}. \quad (3.4.2)$$

The equations look even more alike when multiplying the BSE with \mathcal{C}^T from the right and using $\mathcal{C}^T S^T(q) \mathcal{C} = S(-q)$ on the right-hand side and $\mathcal{C} \mathcal{C}^T = \mathbb{1}$ on the left-hand side. The only difference between the pseudo-scalar meson BSE and the scalar diquark BSE is the different color trace that leads to an extra prefactor of $\frac{1}{2}$ on the right-hand side of the diquark BSE.

The conventions for the diquark and anti-diquark amplitudes read

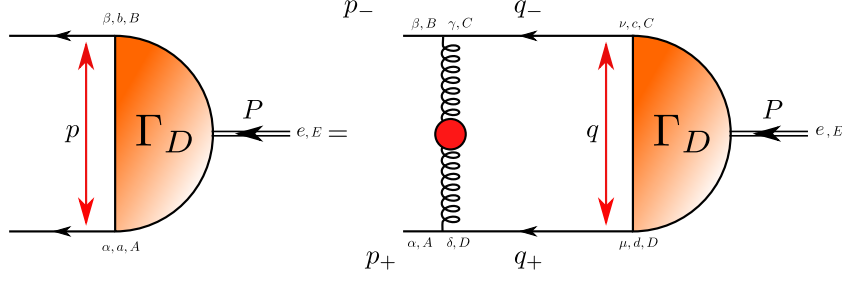


Figure 3.2: Diquark BSE, see Eq. (3.4.3).

$$\begin{aligned}
 & \begin{array}{c} \beta, b, B \\ \leftarrow \\ \Gamma_D \\ \rightarrow \\ \alpha, a, A \end{array} \begin{array}{c} \uparrow \\ p \\ \downarrow \end{array} = \bar{\Gamma}_D(q, P)_{\beta\alpha} \quad , \quad \Gamma_D(q, P)_{\alpha\beta} = \begin{array}{c} \beta, b, B \\ \leftarrow \\ \Gamma_D \\ \rightarrow \\ \alpha, a, A \end{array} \begin{array}{c} \uparrow \\ q \\ \downarrow \end{array} \\
 & \begin{array}{c} \beta, b, B \\ \leftarrow \\ \bar{\Gamma}_D \\ \rightarrow \\ \alpha, a, A \end{array} \begin{array}{c} \uparrow \\ q \\ \downarrow \end{array} = \Gamma_D(-q, P)_{\beta\alpha} \quad , \quad \bar{\Gamma}_D(-q, P)_{\alpha\beta} = \begin{array}{c} \beta, b, B \\ \rightarrow \\ \Gamma_D \\ \leftarrow \\ \alpha, a, A \end{array} \begin{array}{c} \uparrow \\ q \\ \downarrow \end{array} . \\
 \end{aligned} \tag{3.4.3}$$

The second row corresponds to the antidiquark. The relation to the previously defined diquark amplitudes can be derived as follows.

Starting from the upper right amplitude, the lower right can be derived by changing both quarks to antiquarks which is done by insertion of $\mathcal{C}^{(T)}$ matrices to the left and right side of Γ_D :

$$\Gamma_{AD}(q, P)_{\alpha\beta} := (\mathcal{C}\Gamma_D(q, -P)\mathcal{C}^T)_{\alpha\beta} = \tag{3.4.4}$$

$$((\mathcal{C}^T\Gamma_D^T(q, -P)\mathcal{C})^T)_{\alpha\beta} \stackrel{(3.2.5)}{=} \bar{\Gamma}_D(-q, P)_{\beta\alpha}^T = \bar{\Gamma}_D(-q, P)_{\alpha\beta}. \tag{3.4.5}$$

$\Gamma_{AD}(q, -P)$ is the antidiquark amplitude and P is negative because the external momentum points to the right. When carrying out the charge conjugation, the following relations hold:

$$\bar{\Gamma}_M(q, P)_{\beta\alpha} = \{\gamma_5 \overleftarrow{\Gamma}(q, P)\}_{\beta\alpha} \frac{\delta^{AB}}{\sqrt{3}} r_{ba}^u T, \quad (3.4.6)$$

$$\bar{\Gamma}_D(q, P)_{\beta\alpha} = \{\mathcal{C}^T \gamma_5 \overleftarrow{\Gamma}(q, P)\}_{\beta\alpha} \frac{\epsilon^{BAC^T}}{\sqrt{2}} s_{ba}^0 T. \quad (3.4.7)$$

The arrowed amplitudes denote that all signs except for the $\mathbb{1}$ amplitude are switched to minus. The Greek letters on the left-hand side collect the Dirac, flavor and color indices shown on the right-hand side. Because an expansion in even Chebyshev polynomials is applied, the dressing functions stay the same under sign change of the momenta (q, P) .

3.5 Structure of offshell diquark and meson amplitudes

The kernel of the tetraquark BSE contains diquark and meson amplitudes which were calculated from their homogeneous BSE. Unfortunately, the incoming/outgoing momenta of these amplitudes are needed away from the mass-shell whereon the BSE of the meson/diquark was solved. Instead of solving an inhomogeneous BSE for the meson [43] that in principle can resolve properties of the amplitude for arbitrary momenta [53], a different route is taken [54, 20, 38] that utilizes the already calculated onshell solution. The basic idea behind this approach is the assumption that meson and diquark amplitude are dominated by the $i\gamma_5$ -part, while other contributions are suppressed for high momenta P^2 . This corresponds to a point-like diquark and meson in the UV region of P^2 and is achieved by attachment of a suppressing function $g(x)$ to the subleading amplitudes. To amend a possible kinematically singular behavior for $P^2 = 0$, another function $h(x)$ is multiplied to all instances of \hat{P}^μ or $\hat{q} \cdot \hat{P}$ guaranteeing a \sqrt{P} behavior around the mass-shell.

With the definition of the kinematical variable

$$x := \frac{P^2}{M_{M/D}}, \quad (3.5.1)$$

the functions read

$$g(x) = (x + 2)^{-1}, \quad (3.5.2)$$

$$h(x) = -i\sqrt{\frac{x}{x + 2}}. \quad (3.5.3)$$

Both functions evaluated on the mass-shell give $h(1) = g(1) = 1$ and therefore are not changing the onshell properties. One assumes the dressing functions being unaltered in the offshell region.

The problem of $|z| = |\hat{q} \cdot \hat{P}| \geq 1$ for offshell P^2 , rendering the Chebyshev expansion in a strict way not applicable, can be traced back to $P^2 \leq 0$ shifting z into the complex plane and outside of the convergence region $[-1, 1]$ of the Chebyshev polynomials. Due to restrictions in the singularity structure of the kernel, with mainly the meson propagator being the culprit, the tetraquark BSE is solved for positive momenta P^2 only. This confines z to the interval $[-1, 1]$ and legitimates a Chebyshev expansion.

In general the problem of complex z can be amended by discarding all Chebyshev momenta but the 0th order. Another approach is to apply the Chebyshev expansion regardless of the convergence radius if z is only “slightly“ out of bounds. With these approximations, the diquark and meson amplitudes are determined in the whole kinematical region used to solve the tetraquark BSE. Due to the smallness of the higher Chebyshev moments, and the increase in calculation time, all Chebyshev moments but the 0th order were discarded.

3.6 Diquark and meson propagators

Besides the calculation of the offshell meson and diquark amplitudes appearing in the tetraquark DSE, the consistent offshell description of the last section can be used to improve the naive ansatz for the meson and diquark propagators appearing in the tetraquark BSE. The naive (bare) meson and diquark propagator reads

$$D_{M/D} = \frac{1}{p^2 + M_{M/D}^2}. \quad (3.6.1)$$

To improve the propagator the procedure found in [38] is employed. The starting point is Dyson’s equation for the (two-body) T-matrix that reads:

$$T^{(2)}G_0 = K^{(2)}G_0 \left(1 + T^{(2)}G_0\right). \quad (3.6.2)$$

$T^{(2)}$ denotes the two-body T-matrix, $G_0 = SS$ is the product of two (dressed) quark propagators, and $K^{(2)}$ represents the rainbow-ladder kernel which was already used in the meson BSE.

To approximate the T-matrix, it is assumed that the main contribution stems from the parts that contain the poles of the bound state. In this pole approximation, the T-matrix

is written as $T = \Gamma D \bar{\Gamma}$, where the Γ represents the offshell meson or diquark amplitudes and the bared quantities denote charge conjugated amplitudes. The D corresponds to the diquark or meson propagator. After employing the definitions

$$n(x) := \frac{1}{M^2} \bar{\Gamma} S S \Gamma, \quad (3.6.3)$$

$$k(x) := \frac{1}{M^2} \bar{\Gamma} S S K S S \Gamma, \quad (3.6.4)$$

the (inverse) diquark and meson propagator can be extracted from Dyson's equation and has the following form:

$$D^{-1}(P^2) = M^2 \left(\frac{n^2}{k} - n \right). \quad (3.6.5)$$

To circumvent an explicit calculation of the two-loop diagram k , an ansatz also found in [38] is used to model the propagator. The function n is basically the same as the norm integral used in the calculation of the meson BSE, but the external momentum is set to an offshell value. Using the offshell description for the amplitudes, this function is easily calculable. The final inverse meson and diquark propagator is then given by

$$D^{-1}(P^2) = M^2 (-n(x) + \alpha + \beta F(x)). \quad (3.6.6)$$

The functions α, β and $F(x)$ approximate the two-loop contribution $\frac{n^2}{k}$ and follow the ansatz used in [38]:

$$F(x) := \frac{1}{4} \left(1 + \frac{x}{(x+2)^3} \right), \quad (3.6.7)$$

$$\alpha := n(-1), \quad (3.6.8)$$

$$\beta := 1 + \frac{d}{dx} n(x) \Big|_{-1}. \quad (3.6.9)$$

A feature of this description are non-vanishing propagators for $P^2 \rightarrow \infty$. This behavior follows from the Dyson equation for the T-matrix in Eq. (3.6.2), where the kernel diagram dominates, whereas the remainder vanishes due to the vanishing quark propagator. That guarantees the T-matrix in the pole dominance approximation ($T = \Gamma D \bar{\Gamma}$) to stay non-zero for $P^2 \rightarrow \infty$.

Dirac amplitudes	T. moments	m_π [GeV]	m_D [GeV]
1	1	0.119	0.718
2	1	0.138	0.801
3	3	0.142	0.816
4	3	0.138	0.799
4	4	0.137	0.800

Table 3.1: Results for the mass of the meson (m_π) and diquark (m_D). The experimental value for m_π is 138.036 MeV (averaged over the isospin triplet) [10].

3.7 Results for the meson and diquark BSEs

With all ingredients at hand to calculate the meson and diquark amplitudes, the solutions for the onshell momenta are presented. Because the meson and diquark dressing functions are assumed to be the same for offshell and onshell momenta, the knowledge of the onshell dressing functions is sufficient to calculate the offshell amplitudes.

In Fig. 3.3 the results for the onshell pion and diquark amplitudes in the two leading Chebyshev polynomials are shown. As expected, the amplitudes H and G are essentially zero for $p^2 = 0$ because both contain a p -dependent part. The dominant amplitude, by almost one order of magnitude, is the one proportional to $\mathbb{1}$, followed by the one proportional to \not{P} for both diquark and pion. Later on, this is used as motivation to solve the tetraquark BSE via restriction to the two dominant amplitudes (E,F) and 0th order Chebyshev.

An interesting feature of the meson and diquark amplitude is a similar scaling behavior as the one of the quark mass function: the 0th Chebyshev moment of the E and F amplitudes saturate in the infrared and plummet around Λ_{QCD} . This behavior is also apparent in the remaining amplitudes and Chebyshev moments. In the case of the pion, it can be shown analytically that in the chiral limes, the dressing function $E(q^2, 0)$ is proportional to the quark mass function $M(q^2)$ [43]. The sensitivity of the meson and diquark mass to the inclusion of the (G, H) amplitudes and higher Chebyshev momenta is rather small, as can be seen in Tab. 6.1.

To evaluate the amplitudes for arbitrary momenta in the tetraquark BSE, a spline interpolation is used. Because especially the E amplitude with the distinct drop around Λ_{QCD} shows oscillations when applying a spline interpolation directly to the amplitude, the exponent of the amplitudes are interpolated.

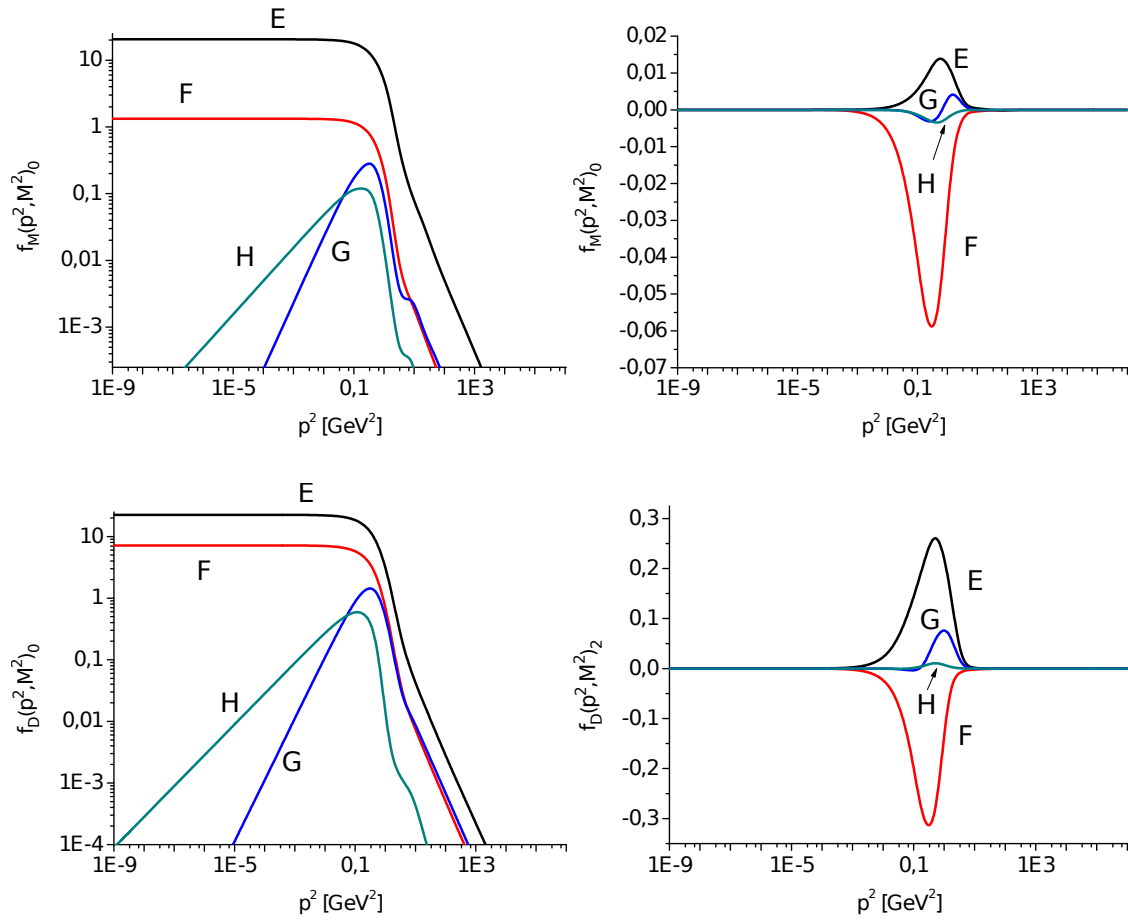


Figure 3.3: Normalized amplitudes of the pseudo-scalar meson (upper row) and scalar diquark (lower row). The left panels show the 0th Chebyshev moments and the right panels the 2nd moments. All odd Chebyshev moments are zero by charge conjugation symmetry. Higher order Chebyshev contributions are even smaller than the 2nd and are not displayed. In the calculation moments up to 6th order were included.

4 Tetraquarks

4.1 Four-body equations

The object that describes a four-quark state is the 8-point Green function. If a tetraquark exists, it would appear as a bound-state pole in that Green function. In order to derive a typical Bethe-Salpeter equation for the tetraquark, one starts from the Dyson equation for G which reads symbolically:

$$G = G_0 + G_0 K^{(4)} G. \quad (4.1.1)$$

$K^{(4)}$ represents a suitable four-body scattering kernel and G_0 is the product of four (dressed) quark propagators. The multiplications in Eq. (4.1.1) represent four-dimensional integrations over the appropriate number of momenta.

A decomposition of $K^{(4)}$ can be seen in Fig. 4.1 [55] where the gray blobs and a implicitly assumed permutation through all the quark lines represent 2PI diagrams. The red blobs indicate three particle irreducible (3PI) and four particle irreducible (4PI) diagrams and are neglected in the following.

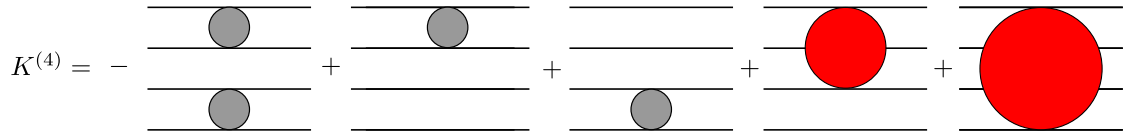


Figure 4.1: four-body Green function (8-point function)

Only considering two-body interactions, one could naively set

$$K^{(4)} = \sum_{i,j} K_{ij}^{(2)} \quad (4.1.2)$$

where i, j label the respective quark lines and the superscript indicates that only 2PI contributions are considered. Upon expanding Eq. (4.1.1) it can be immediately seen that this approach would lead to overcounting because the products of the form $K_{12}K_{34}$ and

$K_{34}K_{12}$ are equal, assuming that the kernel commute. To circumvent this, a term of the form

$$K_{ijkl}^{(4)} := -K_{ij}^{(2)}K_{kl}^{(2)} \quad (4.1.3)$$

has to be added, with the indices $i, j, k, l \in \{1, 2, 3, 4\}$. These indices are mutually different. This yields a scattering kernel of the form

$$\begin{aligned} K^{(4)} &= K_{12}^{(2)} + K_{34}^{(2)} - K_{12}^{(2)}K_{34}^{(2)} \\ &\quad + K_{13}^{(2)} + K_{24}^{(2)} - K_{13}^{(2)}K_{24}^{(2)} \\ &\quad + K_{14}^{(2)} + K_{23}^{(2)} - K_{14}^{(2)}K_{23}^{(2)} \\ &:= K'_{1234} + K'_{1324} + K'_{1423}. \end{aligned} \quad (4.1.4)$$

Starting with Eq. (4.1.1) and dividing G into a sum of a regular part and singular part, a homogeneous Bethe-Salpeter equation for the bound-state amplitude Ψ can be derived [56]:

$$\Psi = K^{(4)}G_0\Psi. \quad (4.1.5)$$

With the same ingredients as used in the meson BSE (namely, the dressed quark propagator from its DSE with the Maris-Tandy effective gluon), this equation is in principle solvable, but technically and numerically demanding. Such a treatment is beyond the scope of this work, hence a different route is taken.

To reduce the problem to a more tractable one, the connection between the kernel and the T-matrix is exploited, cf. Ref. [55]:

$$\mathcal{T}_{a_2} = K'_{a_2} + \mathcal{T}_{a_2}G_0K'_{a_2} \Rightarrow \quad (4.1.6)$$

$$\mathcal{T}_{a_2}G_0 = K'_{a_2}G_0 + \mathcal{T}_{a_2}G_0K'_{a_2}G_0 \Rightarrow \quad (4.1.7)$$

$$\tilde{\mathcal{T}}_{a_2} = \tilde{K}'_{a_2} + \tilde{\mathcal{T}}_{a_2}\tilde{K}'_{a_2}; \quad (4.1.8)$$

$$a_2 \in \{(12)(34), (13)(24), (14)(23)\}.$$

\mathcal{T}_{a_2} denotes the T-matrix of the four-body system with all interactions switched off except between the pair a_2 . For example in $\mathcal{T}_{(12)(34)}$ there are connected diagrams between (12) and (34) individually but none between both pairs. To compactify the notation, the multi-index a_2 was introduced. If not stated otherwise, any primed operator, amplitude

etc. with an index $\in \{1, 2, 3\}$ corresponds to the appropriate multi-index given in the definition of a_2 above. The accent tilde denotes quantities that were folded with G_0 from the right. In a first step and analogous to the 3-body case, Eq. (4.1.5) is reformulated in terms of the so-called Faddeev amplitudes, where the replacement

$$\tilde{K}'_i \Psi =: \Psi'_i \quad (4.1.9)$$

is employed. Afterwards, Ψ is multiplied in a functional sense to the left-hand side and right-hand side of Eq. (4.1.8). With the definition of the Faddeev amplitudes given above, the following relation between amplitudes and \mathcal{T}_{a_2} can be established:

$$\Psi'_i = \mathcal{T}_i (\Psi'_j + \Psi'_k), \quad i \neq j \neq k. \quad (4.1.10)$$

Except for the omission of the genuine 4- and 3-body parts, this equation is still identical to Eq. (4.1.9) with only the kernel replaced by the (unknown) T-matrix.

In principle the, T-matrix can be calculated by solving a complicated set of operator equations [55]. Because the solutions of these operator equations are out of scope of this work, the following two ansätze are used, justified by the assumption that \mathcal{T}_{a_2} should be dominated by the two-body T-matrices. In analogy to the form of the kernel (4.1.4), the T-matrix in setup (1) is chosen to have the same structural form

$$\mathcal{T}_{a_2} := -T_{ij}^{(2)} T_{kl}^{(2)} + T_{(ij)}^2 + T_{(kl)}^2. \quad (4.1.11)$$

Setup (2), on the other hand, omits the single T-matrices but keeps the sign for the T-matrix product:

$$\mathcal{T}_{a_2} := -T_{ij}^{(2)} T_{kl}^{(2)}. \quad (4.1.12)$$

The consequences of a different sign is discussed in the results chapter.

The second setup was chosen from the more naive point of view that the tetraquark is built up by a diquark-(anti)diquark or meson pair, and so the tetraquark T-matrix should be dominated by the product of the two-body T-matrices. In analogy to the nucleon Faddeev equation and its reduction to a quark-diquark picture [38], it is assumed that the two-body T-matrix, containing a bound state, is dominated by the pole contribution:

$$T_{ij}^{(2)}(p, P) := \Gamma_{ij}(p, P) D(P^2) \bar{\Gamma}_{ij}(p, P). \quad (4.1.13)$$

Γ encodes the respective meson or diquark amplitude and D the corresponding propagator. Quantities with a bar indicate charge conjugated amplitudes. To finally arrive

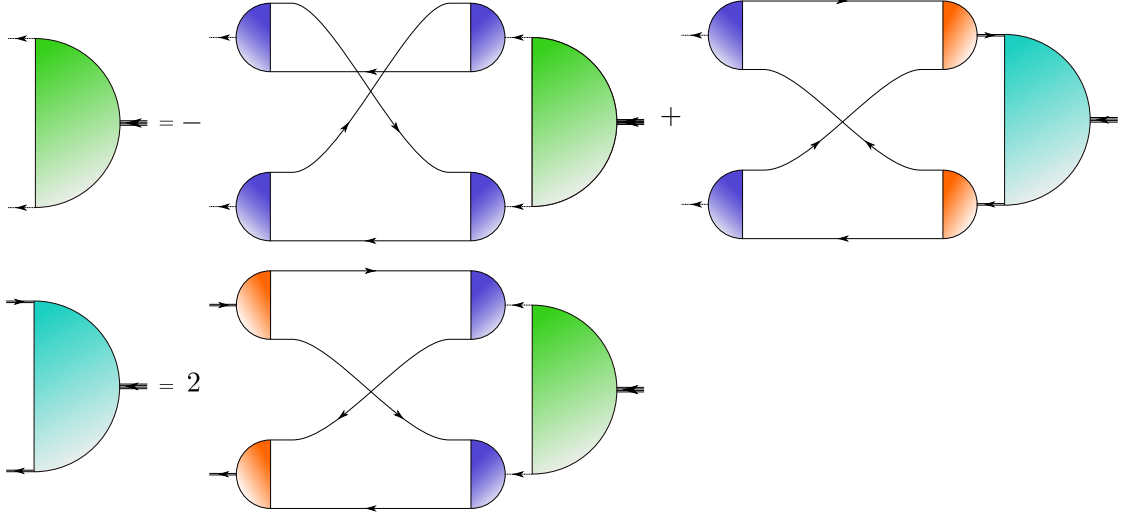


Figure 4.2: Tetraquark BSE in the meson-meson/antidiquark-diquark picture.

at a two-body equation, an ansatz is applied that relies on the assumption that the internal momenta dependence of Ψ_i can be separated into a product. Following the meson-meson/antidiquark-diquark picture, the separated parts are identified with two meson or a diquark and antidiquark offshell amplitude. This separability ansatz plugged into the Faddeev amplitude yields

$$\Psi'_{a_2} := \Gamma_{(ij)}^a(q_1, Q_1) D_{(ij)}^a(Q_1) \Gamma_{(kl)}^b(q_2, Q_2) D_{(kl)}^b(Q_2) \Phi_{a_2}(q, P)^{ab}. \quad (4.1.14)$$

The index a_2 denotes the three Faddeev amplitudes and (a, b) contain all flavor and color indices. For $a_2 = (12)(34)$, Γ stands for diquark-antidiquark amplitudes and D for the diquark propagator; in the case of $a_2 \in \{(13)(24), (14)(23)\}$ the involved objects are of mesonic nature. The separated internal momenta are (q_1, q_2) and correspond to the relative momenta of the (anti)diquarks and mesons. The momenta (Q_1, Q_2) can take arbitrary values and are the reason why an offshell description for the meson and diquark amplitudes is necessary.

Φ itself is a flavor and color singlet and has the structure of scalar with quantum number $J^P = 0^+$. A detailed description of the flavor, color and momentum structure can be found in chapter 4.3.

Using the offshell ansatz for the meson and diquark amplitudes introduced in chapter 3.5 and the dressed quark propagator from its DSE in rainbow-ladder truncation, the tetraquark BSE in Fig. 4.2 is fully determined up to a normalization constant. The normalization of the onshell tetraquarks can be derived in analogy to Eq. (3.1.8) and

(3.1.9). A diagrammatic derivation of the equation in Fig. 4.2 is given in the following section.

4.2 Diagrammatic derivation

To derive the tetraquark BSE, the Faddeev amplitudes and the two-body T-matrices are depicted in a graphical form. This procedure improves the readability of the involved equations and simplifies the derivation.

Starting with Eq. (4.1.10) and Eq. (4.1.11), the following graphical representations are used for the tetraquark amplitudes and the two-body T-matrices:

$$\Psi'_1 := \text{[Diagram 1]} \quad \Psi'_2 := \text{[Diagram 2]} \quad \Psi'_3 := \text{[Diagram 3]}, \quad (4.2.1)$$

$$\begin{aligned} \mathcal{T}_1 &:= - \text{[Diagram 1.1]} + \text{[Diagram 1.2]} + \text{[Diagram 1.3]} \\ \mathcal{T}_2 &:= - \text{[Diagram 2.1]} + \text{[Diagram 2.2]} + \text{[Diagram 2.3]} \\ \mathcal{T}_3 &:= - \text{[Diagram 3.1]} + \text{[Diagram 3.2]} + \text{[Diagram 3.3]} \end{aligned} \quad (4.2.2)$$

The color of the blobs indicates the type of T-matrix. The orange ones stand for a (anti)quark-(anti)quark correlation and the blue ones for a quark-antiquark correlation. Light blue semi-circles represent a diquark-antidiquark tetraquark and green ones the meson-meson amplitudes. To indicate which quarks are interacting with each other, the quark lines in the T-matrix are aligned in the same order as in the tetraquark amplitude. The wiggly lines in Eq. (4.2.2) do not represent a simple gluon exchange, as could be inferred on a first glance, but incorporate the full interaction between the involved quarks. Subsequently it is assumed that this two-pair interaction is furthermore dominated by the meson and (anti)diquark poles respectively. This assumption is one-to-one with the separation ansatz in Eq. (4.1.14).

Without loss of generality, it is assumed that the quarks have the ordering $\bar{q}\bar{q}qq$ in the amplitudes in Eq. (4.2.1). The antisymmetry in the qq and $\bar{q}\bar{q}$ pair is implicitly included in the definition. As it will be seen, this symmetry condition reduces the number of equations to two. The set of pictograms shown in Eq. (4.2.1) and Eq. (4.1.8) is now inserted into Eq. (4.1.10) with all internal integrals implicitly included:

$$\begin{aligned}
\Psi'_1 := & \left(\begin{array}{c} \text{Diagram 1} \\ \text{Diagram 2} \\ \text{Diagram 3} \end{array} \right) \left(\begin{array}{c} \text{Diagram 4} \\ \text{Diagram 5} \end{array} \right) = \\
& = - \left(\begin{array}{c} \text{Diagram 6} \\ \text{Diagram 7} \end{array} \right) + \left(\begin{array}{c} \text{Diagram 8} \\ \text{Diagram 9} \end{array} \right) + \left(\begin{array}{c} \text{Diagram 10} \\ \text{Diagram 11} \end{array} \right) - \left(\begin{array}{c} \text{Diagram 12} \\ \text{Diagram 13} \end{array} \right) \\
& + \left(\begin{array}{c} \text{Diagram 14} \\ \text{Diagram 15} \end{array} \right) + \left(\begin{array}{c} \text{Diagram 16} \\ \text{Diagram 17} \end{array} \right)
\end{aligned}
\tag{4.2.3}$$

$$\begin{aligned}
\Psi'_2 := & \left(\begin{array}{c} \text{Diagram 1} \\ \text{Diagram 2} \\ \text{Diagram 3} \end{array} \right) \left(\begin{array}{c} \text{Diagram 4} \\ \text{Diagram 5} \end{array} \right) = \\
& = - \left(\begin{array}{c} \text{Diagram 6} \\ \text{Diagram 7} \end{array} \right) + \left(\begin{array}{c} \text{Diagram 8} \\ \text{Diagram 9} \end{array} \right) + \left(\begin{array}{c} \text{Diagram 10} \\ \text{Diagram 11} \end{array} \right) - \left(\begin{array}{c} \text{Diagram 12} \\ \text{Diagram 13} \end{array} \right) \\
& + \left(\begin{array}{c} \text{Diagram 14} \\ \text{Diagram 15} \end{array} \right) + \left(\begin{array}{c} \text{Diagram 16} \\ \text{Diagram 17} \end{array} \right)
\end{aligned}
\tag{4.2.4}$$

$$\begin{aligned}
\Psi'_3 := & \left(\begin{array}{c} \text{Diagram 1} \\ \text{Diagram 2} \\ \text{Diagram 3} \end{array} \right) \left(\begin{array}{c} \text{Diagram 4} \\ \text{Diagram 5} \end{array} \right) = \\
& = \begin{array}{c} \text{Diagram 6} \\ \text{Diagram 7} \\ \text{Diagram 8} \\ \text{Diagram 9} \\ \text{Diagram 10} \\ \text{Diagram 11} \end{array}
\end{aligned}
\tag{4.2.5}$$

The third equation is redundant and yields the same equation as the one for Ψ'_2 . In order to reduce the four-body problem to a two-body problem, the pole dominance assumption from Eq. (4.1.13) is applied for the T-matrices, and the BSE amplitudes are replaced by the separated ansatz of (4.1.14). Both read in a graphical notation:

$$\begin{array}{c} \text{Diagram 12} \end{array} = \begin{array}{c} \text{Diagram 13} \end{array} \begin{array}{c} \text{Diagram 14} \end{array} ; \quad \begin{array}{c} \text{Diagram 15} \end{array} = \begin{array}{c} \text{Diagram 16} \end{array} \begin{array}{c} \text{Diagram 17} \end{array}
\tag{4.2.6}$$

$$\begin{array}{c} \text{Diagram 18} \end{array} := \begin{array}{c} \text{Diagram 19} \end{array} ; \quad \begin{array}{c} \text{Diagram 20} \end{array} := \begin{array}{c} \text{Diagram 21} \end{array}$$

$$\begin{array}{c} \text{Diagram 22} \end{array} := \begin{array}{c} \text{Diagram 23} \end{array}
\tag{4.2.7}$$

To derive the symmetry factors in front in the upper line, the order of $\bar{q}\bar{q}qq$ in the upper amplitudes is changed to $\bar{q}q\bar{q}q$ so that the quark lines connected by a 'wiggly' line are

next to each other. The absolute position of the quark line end does not change in this process. This exchange of quarks complies with the Pauli principle and yields a minus sign whenever two quarks or antiquarks are interchanged. The topmost left amplitude in Eq. (4.2.7) acquires two interchanges, one is a $q\bar{q}$ interchange and the other one a qq interchange accompanied by a the minus sign. The right amplitude needs only one $\bar{q}q$ interchange resulting in an overall positive sign. The lower diagram has already the correct ordering.

Upon inserting these diagrams in Eqs. (4.2.3) - (4.2.5), the system has still a structural flaw. Namely, the fact that there are diagrams which are closed in the sense that there are no open quark lines, whereas other diagrams have two open quark lines. To cast it into a more tractable problem, both sides are multiplied (in an integrational sense) by the following diagrams:

(4.2.8)

This has two effects. On one hand, the aforementioned open quark lines are now closed, and on the other hand each diagram collects an additional factor. These factors are denoted as $N_M^{\uparrow\downarrow}(P^{\uparrow\downarrow})$ and $N_D^{\uparrow\downarrow}(P^{\uparrow\downarrow})$. The arrows encode the momentum dependencies with $P^{\uparrow} = P - \frac{1}{2}p$ the momentum of the upper-left external leg of the tetraquark and $P^{\downarrow} = P + \frac{1}{2}p$ the lower-left one. The pictographical representation of these prefactors reads

(4.2.9)

The long lines on the right-hand side indicate that the factors already include the propagator of the meson or diquark respectively.

The diagrams are essentially the same as those calculated for the normalization of the meson and diquark BSE. Because they depend only on unintegrated momenta, a calculation in advance is straightforward. It turns out that a straight forward calculation of the prefactors, using the offshell prescription of the BSE amplitudes, has a serious flaw:

They exhibit a structure that looks like a dipole singularity for positive P^2 . For a more in-depth analysis and a possible cure, see section 4.4.

Putting all together yields the following set of equations, where for the setup of Eq. (4.1.12) that omits the single two-body T-matrices, the brackets equal -1 :

$$\begin{aligned}
 & \left[\text{Green semi-circle} \right] = - \left(-1 + \frac{N_M^\uparrow(P) + N_M^\downarrow(P)}{N_M^\uparrow(P)N_M^\downarrow(P)} \right) \left[\text{Diagram 1} \right] \\
 & \left[\text{Cyan semi-circle} \right] = + \left(-1 + \frac{N_D^\uparrow(P) + N_D^\downarrow(P)}{N_D^\uparrow(P)N_D^\downarrow(P)} \right) \left[\text{Diagram 2} \right] \\
 & \left[\text{Cyan semi-circle} \right] = 2 \left(-1 + \frac{N_M^\uparrow(P) + N_M^\downarrow(P)}{N_M^\uparrow(P)N_M^\downarrow(P)} \right) \left[\text{Diagram 3} \right]
 \end{aligned}
 \tag{4.2.10}$$

4.3 Four-body kernels

In this section the four-body kernels depicted in Eq. (4.2.10) are computed in detail, see Figs. 4.3 , 4.4 and 4.5 for a detailed graphical representation. The following notational conventions are used: The subscripts $+$ and $-$ below the momentum variables arise from the momentum partitioning in the bound state amplitudes and have to be read as

$$q_+ := +q + \frac{1}{2}P, \quad q_- := -q + \frac{1}{2}P.
 \tag{4.3.1}$$

$P := q_- + q_+$ is the center of mass (cms) momentum of the involved object (meson, diquark, tetraquark) and $q := \frac{q_+ - q_-}{2}$ denotes the relative momentum of an equal mass two-body system. All momenta flowing from left to right have a positive sign, the other direction picks up a negative sign. The (dressed) quark propagator meets the usual Feynman rule in index notation:

$$\begin{aligned}
S(-p)_{\beta\alpha} &= \overrightarrow{\alpha \quad p \quad \beta} \\
S(p)_{\alpha\beta} &= \overleftarrow{\alpha \quad p \quad \beta}
\end{aligned}
\tag{4.3.2}$$

The notation for the meson and diquark amplitudes was introduced in chapters 3.3 and 3.4. The following definitions for the momenta, which can be derived from momentum conservation at each vertex, are used for all three kernels:

$$\begin{aligned}
q_- &= -q + \frac{1}{2}P \quad , & q' &= q'' + p \quad , & (4.3.3) \\
q_+ &= q + \frac{1}{2}P \quad , & q''' &= q'' - \frac{1}{2}q + \frac{1}{2}p \quad , \\
p_- &= -p + \frac{1}{2}P \quad , & q'''' &= q'' + \frac{1}{2}q + \frac{1}{2}p \quad , \\
p_+ &= p + \frac{1}{2}P \quad , & & &
\end{aligned}$$

$$\begin{aligned}
q''_- &= -q'' + \frac{1}{2}q_- \quad , & (4.3.4) \\
q''_+ &= q'' + \frac{1}{2}q_- \quad , \\
q'_- &= -q' + \frac{1}{2}q_+ \quad , \\
q'_+ &= q' + \frac{1}{2}q_+ .
\end{aligned}$$

As in the meson case, the momentum sharing parameter $\eta = \frac{1}{2}$ between the mesons/diquarks and the attached quarks is chosen. This choice ensures that the relative momenta of the meson and diquark amplitudes stay real and thereby reduces the numerical effort significantly because otherwise a two-dimensional evaluation in the real and imaginary direction of the relative momentum would be necessary.

The diagrams are genuinely two-loop with q and q'' as the momenta integrated over. A suitable integration method to handle these two-loop integrals is given in chapter 5.2.

4.3.1 Meson-meson kernel

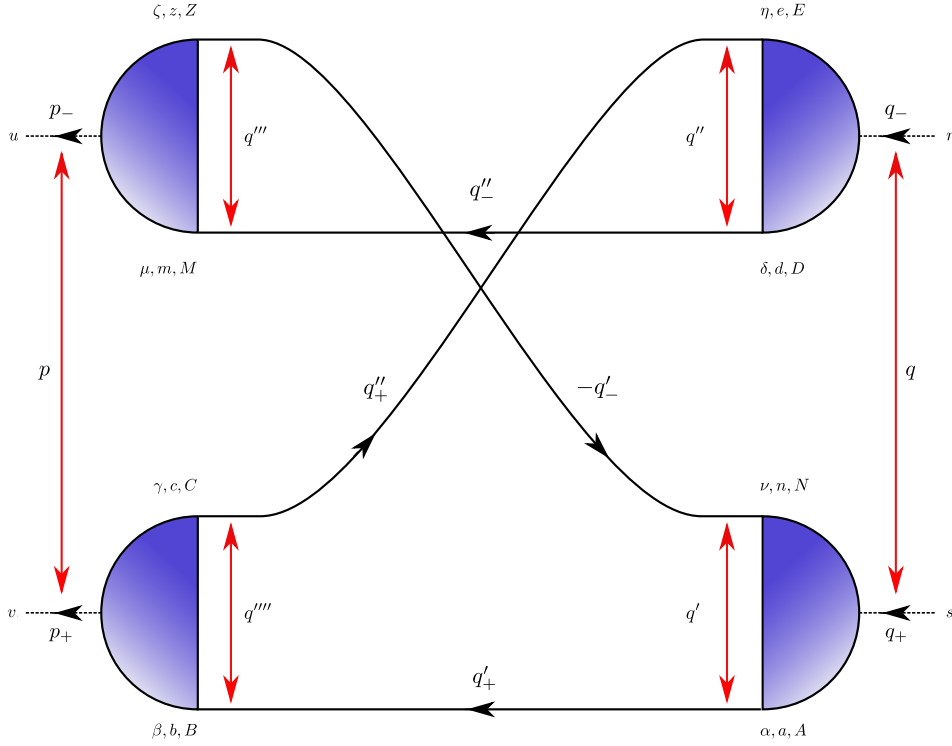


Figure 4.3: Meson-meson kernel

In the meson-meson kernel, the amplitudes already have the correct order. With the help of the relations $\{\gamma_5, \gamma^\mu\} = 0$ and $(\gamma_5)^2 = \mathbb{1}$ to eliminate all γ_5 matrices, the Dirac trace can be written in the following form:

$$K_{MM}(P, p, q, q'') := \text{Tr} \left[S(q'_+) \Gamma_M(-q''', -p_+) S(q''_-) \right. \\ \left. \times \overleftrightarrow{\Gamma}_M(q'', q_-) S(q''_+) \Gamma_M(-q''', -p_-) S(q'_-) \overleftrightarrow{\Gamma}_M(q', q_+) \right]. \quad (4.3.5)$$

The Γ_M are offshell meson amplitudes modulo $i\gamma_5$. The double arrow above the amplitudes indicates that the sign of all basis elements but the $\mathbb{1}$ is reversed. The color and flavor traces can be calculated in advance:

$$C_{MM} := \frac{\delta^{AN} \delta^{NM} \delta^{ME} \delta^{EA}}{\sqrt{3}} = \frac{\delta^{AA}}{9} = \frac{1}{3} \quad (4.3.6)$$

$$F_{MM} := \sum_s r_s^{an} \bar{r}_v^{nm} r_s^{me} \bar{r}_u^{ea} = -\frac{1}{2} \delta^{vu}. \quad (4.3.7)$$

The indices $s, v, u \in \{\pm, 0\}$ are chosen in such a way that the tetraquark has an electrical charge of zero. Taking into account the minus in front of the corresponding BSE diagram, the overall sign is positive and the combined color, flavor and sign factor becomes $\frac{1}{6}$. The bar over the flavor matrices denotes transposition.

4.3.2 Meson-diquark kernel

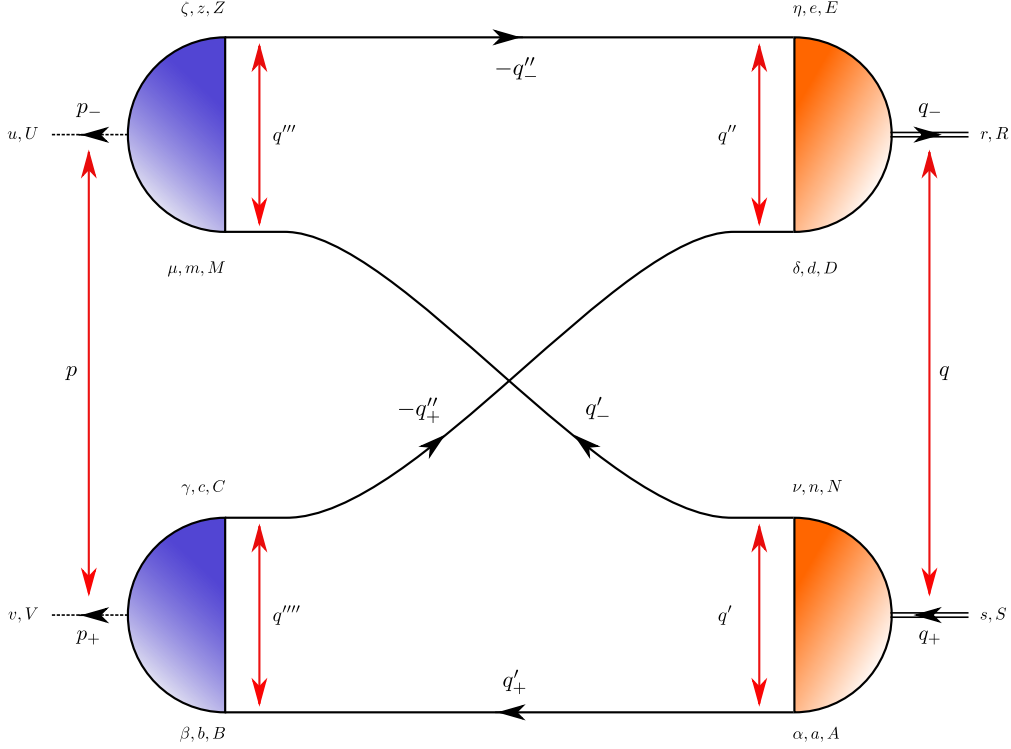


Figure 4.4: Meson-diquark kernel

Writing down the trace for the diquark-meson kernel, one stumbles over charge conjugation matrices \mathcal{C} and amplitudes that do not have the right ordering of matrix indices. To show the general procedure, a detailed calculation to handle these occurrences is presented. The factors of i in front of all meson amplitudes are removed due to cancellation ($i^4=1$). As before, the bar over the amplitudes correspond to charge conjugation. The quark propagator obeys the following charge conjugation property:

$$\mathcal{C}S^T(p)\mathcal{C}^T = S(-p), \quad (4.3.8)$$

which can be deduced directly from the transformation property of the γ^μ matrix [25]. Using the indices defined in Fig. 4.4, the Dirac trace can be displayed with the Dirac

matrix indices explicitly stated:

$$K_{MD}(P, p, q, q'') := \text{Tr} \left[S(q'_+)_{\beta\alpha} \bar{\Gamma}_M(q''''', p_+)_{\gamma\beta} S(-q''_-)_{\delta\gamma} \bar{\Gamma}_D(-q'', q_-)_{\delta\eta} S(-q''_+)_{\eta\xi} \right. \\ \left. \bar{\Gamma}_M(-q''''', p_-)_{\xi\mu} S(q'_-)_{\mu\nu} \Gamma_D(q', q_+)_{\alpha\nu} \right]. \quad (4.3.9)$$

Upon simultaneously interchanging the matrix indices and using the transposed quantities, as well as using $\Gamma_D^T(q', q_+) = -\Gamma_D(-q', q_+)$ and the explicitly stating the γ_5 and \mathcal{C} matrices and with the rules for the transposition of the meson/diquark amplitudes, the trace can be written as

$$K_{MD}(P, p, q, q'') := -\text{Tr} \left[S^T(q'_+) \mathcal{C}^T \gamma_5 \Gamma_M(-q''''', -p_+) \mathcal{C} S^T(-q''_-) \mathcal{C}^T \gamma_5 \right. \\ \left. \overleftrightarrow{\Gamma}_D(-q'', q_-) S(-q''_+) \gamma_5 \overleftrightarrow{\Gamma}_M(-q''''', p_-) S(q'_-) \gamma_5 \Gamma_D(-q', q_+) \mathcal{C} \right] = \\ = -\text{Tr} \left[S(q'_+) \Gamma_M(-q''''', -p_+) S(q''_-) \right. \\ \left. \overleftrightarrow{\Gamma}_D(q'', q_-) S(q''_+) \Gamma_M(-q''''', -p_-) S(q'_-) \overleftrightarrow{\Gamma}_D(q', q_+) \right]. \quad (4.3.10)$$

In the last step all occurrences of γ_5 were eliminated. The flavor and color traces yield

$$C_{MD} := \frac{\delta^{SR} \delta^{DA} \delta^{NE} \epsilon^{NAS} \epsilon^{EDR}}{6} = \frac{\epsilon^{NAS} \epsilon^{NAS}}{6} = 1, \quad (4.3.11)$$

$$F_{MD} := r_v^{bc} s_0^{ce} \bar{r}_u^{em} \bar{s}_0^{mb} = -\frac{1}{2} \delta^{uv}. \quad (4.3.12)$$

As in the case of the meson-meson kernel, the combination of all factors from the various traces and the BSE itself gives a positive factor. The numerical value is $\frac{1}{2}$.

4.3.3 Diquark-meson kernel

The kernel for the diquark-meson diagram can be calculated in the same manner as the meson-diquark kernel. The result for the Dirac trace gives

$$K_{DM}(P, p, q, q'') := -\text{Tr} \left[S(q'_+) \Gamma_D(-q''''', -p_+) S(q''_-) \right. \\ \left. \overleftrightarrow{\Gamma}_M(q'', q_-) S(q''_+) \Gamma_D(-q''''', -p_-) S(q'_-) \overleftrightarrow{\Gamma}_M(q', q_+) \right]. \quad (4.3.13)$$

The flavor and color traces read

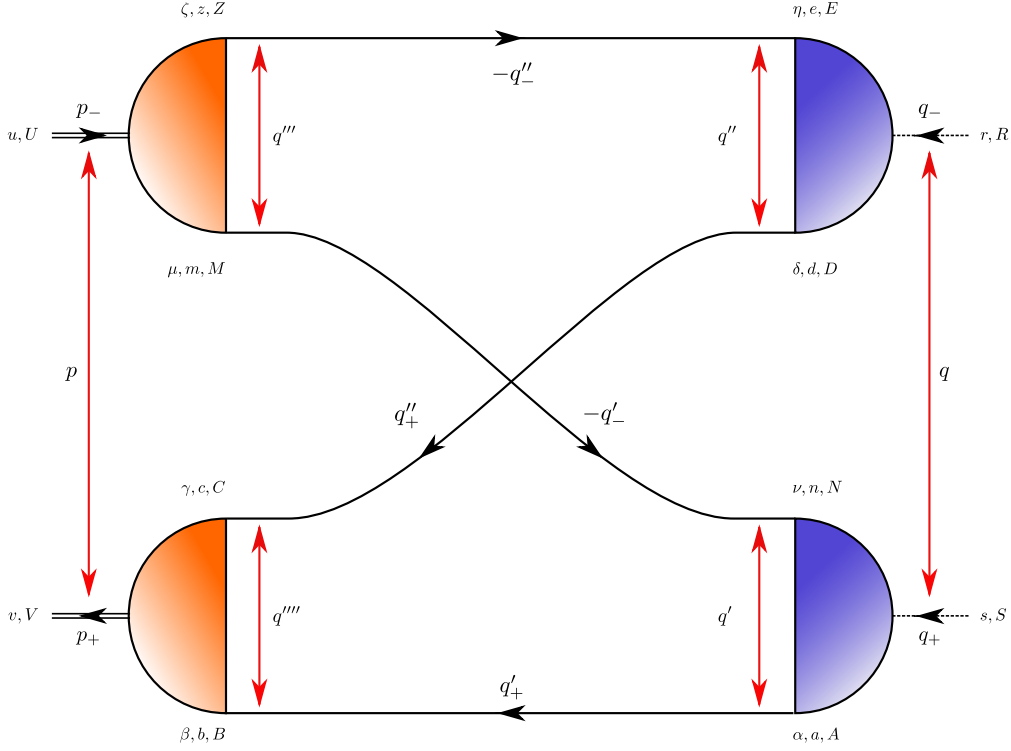


Figure 4.5: Diquark-Meson kernel

$$C_{DM} := \frac{\delta^{CZ} \delta^{BM} \epsilon^{BCV} \epsilon^{MZU}}{6} = \frac{\epsilon^{BCV} \epsilon^{BCU}}{6} = \frac{1}{3} \delta^{UV}, \quad (4.3.14)$$

$$F_{DM} := \sum_s s_0^{bc} r_s^{ce} \bar{s}_0^{em} \bar{r}_s^{mb} = -\frac{3}{2}. \quad (4.3.15)$$

After combining all prefactors, the overall factor equals 1.

The explicit form of the Dirac traces of the kernels is a huge expression. Even by restriction to the two dominant amplitudes of diquark and meson (E, F), the kernels fill a couple of pages, so a detailed notation will be passed on. For the explicit calculation of the traces the *Mathematica* package *FeynCalc* [57] was used. It turned out to be the faster and more manageable strategy to evaluate the traces in the most general form without specifying the momentum dependencies on p, P, q, q'' and corresponding angular variables, and insert the explicit dependencies *after* the evaluation of the trace. It is interesting to note that the kernels given above are, up to some prefactors, similar to the corresponding decay diagrams into $\pi\pi$. If the tetraquark amplitude were known on the mass-shell the diagrams above could be used to calculate the width.

Another interesting feature can be seen in Eq. (4.2.10): the diquark-antidiquark ampli-

tude on the right-hand side of the first line can be replaced by the expression of the second line. This transforms the tetraquark BSE into a form that reads symbolically

$$\Psi_M = K_{MM}\Psi_M + K_{MD}K_{DM}\Psi_M. \quad (4.3.16)$$

Ψ_M denotes the meson-meson tetraquark amplitude. This underlines the role of the diquark-antidiquark amplitude as a correlation that is 'confined' within the tetraquark. In order to be able to distinguish the contributions of meson-meson and diquark-antidiquark amplitudes, the above replacement above was not applied but the original system of Eq. (4.2.10) was solved.

4.4 Prefactors in the tetraquark BSE

In this section, the prefactors that were first encountered in the derivation of the tetraquark BSE (see Eq. (4.2.10)) are calculated and discussed. Two approaches to handle the occurring singularities are introduced and calculated.

These prefactors read

$$\alpha_{M/D}(P) := \left(-1 + \frac{N_{M/D}^\uparrow(P) + N_{M/D}^\downarrow(P)}{N_{M/D}^\uparrow(P)N_{M/D}^\downarrow(P)} \right). \quad (4.4.1)$$

They are calculated by evaluation of the diagrams in Eq. (4.2.9), utilizing the ansatz for the offshell amplitudes introduced in section 3.5. The result indicates that the factors feature a singularity on the positive P^2 axis, see Fig. 4.6.

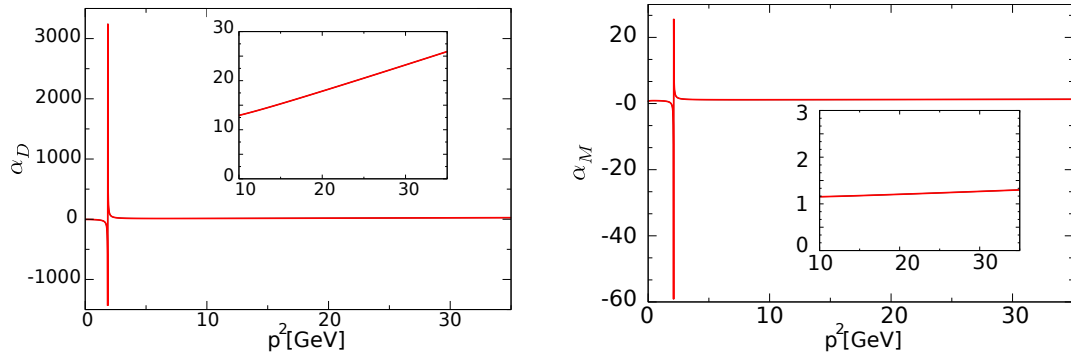


Figure 4.6: Prefactors of the diquark contribution $\alpha_D(P)$ (left) and $\alpha_M(P)$ (right) to the tetraquark BSE. The angular variable z is set to zero.

The singularities reside around 2 GeV^2 which is fairly far away from the expected mass

Setup	Amplitude	A_0	A_1	A_2	A_3
1	Meson	53.0288	1.43832	0.89299	0.363514
2	Meson	53.0288	2.4216	0	0
1	Diquark	0.696636	1.39305	1.13982	0.578506
2	Diquark	0.696636	2.4392	0	0

Table 4.1: Fit parameters for $n(x)$ using Eq. (4.4.3) as fit function. Setup 1 employs a best fit and setup 2 a simple fit to $1/(1 + P^2)$. The underlying meson/diquark BSE was solved for all amplitudes and three Chebyshev moments.

of the tetraquark. The problem can be seen from the momentum structure of P

$$P = P_4 \pm \frac{1}{2}p_4, \quad (4.4.2)$$

with P_4 denoting the tetraquark mass and p_4 the relative momentum inside the integral. The variable p_4 lies in the range between IR- and UV-cutoff which are typically in the order of $p_{IR}^2 \approx 10^{-6}$ GeV and $p_{UV}^2 \approx 10^9$ GeV. Thus, the region with the singularity is sampled during the calculation, rendering the system of equations ill-defined. To cure this undesired feature, three different setups were applied.

The first one calculates n for real positive P^2 below the zero crossing and fits the resulting curve by a positive definite function. For simplicity,

$$\frac{A_0}{1 + A_1(P^2)^1 + A_2(P^2)^3 + A_3(P^2)^5} \quad (4.4.3)$$

was chosen. The exponents (1, 3, 5) for P^2 were selected to guarantee positive coefficients. In the second setup, was function above defined was restricted to $A_2 = A_3 = 0$. The resulting fit is not as good as the first one but preserves the linear behavior of α for high P^2 , see Fig. 4.6. The third setup is based on the replacement of $KSS\Gamma$ with $\lambda\Gamma$ in Eq. (3.6.2) which assumes that a solution of the onshell BSE ($KSS\Gamma = \lambda\Gamma$) is sufficient to resolve also properties for offshell P^2 . In this case, λ is the eigenvalue of the homogeneous BSE with an offshell external momentum P^2 . Upon solving Dyson's equation this yields

$$D_{M/D}^{-1}(x) = -n(x) \left(\frac{1}{\lambda} - 1 \right). \quad (4.4.4)$$

and subsequently

$$N_{M/D}^{\uparrow\downarrow}(P) = nD = -\frac{\lambda_{M/D}^{\uparrow\downarrow}(P)}{1 - \lambda_{M/D}^{\uparrow\downarrow}(P)} \quad (4.4.5)$$

$$\alpha_{M/D}(P) := 1 - \left(\frac{1}{\lambda_{M/D}^\downarrow(P)} + \frac{1}{\lambda_{M/D}^\uparrow(P)} \right). \quad (4.4.6)$$

This eliminates the singularity for $\lambda \leq 1$, which happens for $P^2 \geq m_{\pi/D}^2$. The eigenvalue λ behaves properly in the offshell region and does not cross the zero line. Nevertheless an ambiguity still remains in the proper definition of the meson and diquark propagator. Namely a calculation of the meson/diquark propagator based on (4.4.5) is not viable since the singularity for positive P^2 is merely shifted to the propagator upon dividing by $n(x)$. To still be able to test this ansatz, the meson and diquark propagators of Eq. (3.6.6) are applied.

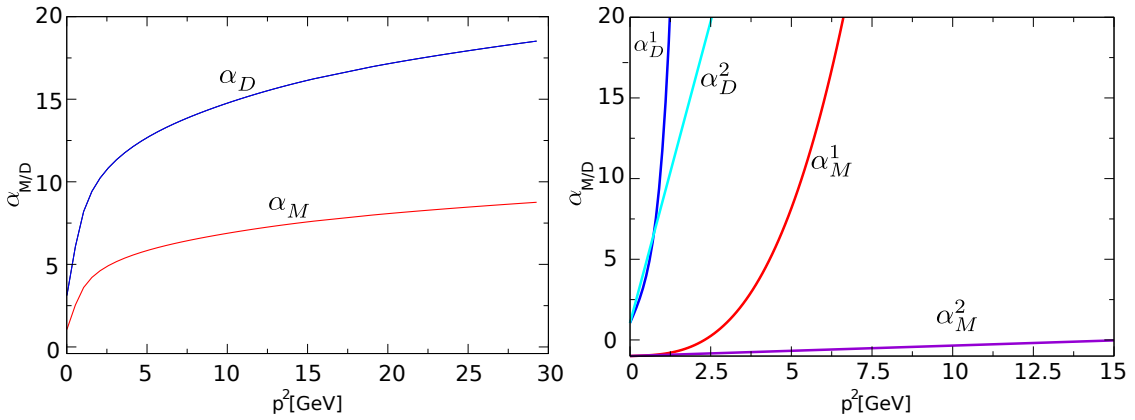


Figure 4.7: *Left panel:* The prefactors calculated by means of the eigenvalue λ , see Eq. (4.4.6). To simplify the calculation the angle between P_4 and p_4 was set to zero, mimicking the case where only the 0th Chebyshev momentum of the tetraquark amplitude is calculated. *Right panel:* A fit of the functions $n(P^2)$ is used to calculate the prefactors. The superscript '1' denotes the best fit of $n(P^2)$ in the region before the zero crossing and '2' the case where a simpler function was chosen to yield a linear prefactor.

As can be seen in Fig. 4.7, the behavior of all three setups is very different. Since the function $n(x)$ was fitted in the first setup by an irrational function of higher order, the inverse has the form of some higher order polynomial, depicted in the right-hand side of Fig. 4.7. The second setup that uses the simple fit does not exhibit this feature but rises linearly. The behavior of the factor that uses the eigenvalues of the meson/diquark BSE looks completely different. The discrepancy can be traced back to their different conceptual origins.

While the first two setups are based on an explicit ansatz for the offshell meson and

diquark amplitudes and require a fitting procedure to remove unwanted singularities, the third setup features no singularities but relies on the assumption that the onshell BSE yields a meaningful amplitude in the offshell regime. Both procedures are to some extent arbitrary and employed to explore the behavior of the tetraquark BSE, such that deficiencies can be ultimately located in the offshell description of the meson and diquark amplitudes.

apart from those the singularities the prefactor $\alpha_{M/D}$ calculated with the unfitted $n(P^2)$, shows a linearly rising behavior beyond the pole, see Fig. 4.6. This behavior is (qualitatively) recovered in the second setup that uses $\frac{A_0}{1+A_1 P^2}$ as fit function and is also seen in the setup that employs the eigenvalue of the meson BSE.

The influence of these different setups on the tetraquark BSE is discussed in the result chapter. Despite their quite different behavior, it will turn out that their impact on the tetraquark mass is surprisingly small.

5 Numerics

In this chapter numerical details are collected that were employed to solve the Bethe-Salpeter equations for the meson, diquark and tetraquark bound-state amplitudes.

5.1 The BSE as eigenvalue problem

The homogeneous meson BSE and the tetraquark BSE have the same structural form of equation

$$K\Psi = \Psi, \quad (5.1.1)$$

where the multiplication is understood as an integral over all internal momenta. The functional dependency of all amplitudes is given by

$$\Psi = \Psi(p^2, P^2, z) \quad (5.1.2)$$

and an expansion in Chebyshev polynomials is applied for the angular variable z . The remaining dependency on p^2 after discretization of the integrals is expressed in the following matrix equation

$$\Psi_{i_D, i_T, i_p} = \sum_{j_D, j_T, j_p} w_{j_p} \int dp_{in} K(p_{in})_{i_D, i_T, j_D, j_T} \Psi_{j_D, j_T, j_p}. \quad (5.1.3)$$

The summation index $i_D \in \{1, 2, 3, 4\}$ enumerates the respective Dirac basis element in the meson case and distinguishes between meson-meson and diquark-antidiquark amplitude in the tetraquark case. The index $i_T \in \{1, \dots, T_n\}$ lists the Chebyshev moment, and $i_p \in \{1, \dots, p_n\}$ denotes the momenta of the n th order Gauss-Legendre quadrature algorithm with w_{j_p} representing the corresponding integration weight. In the following all these indices are included in the multi-index $(i), (j)$. The remaining expression $\int dp_{in} K(p_{in})$ is a shorthand notation and contains the rest of the internal integrations, the color and flavor traces, the summation applied to obtain the Chebyshev expansion, and the tracing to project out the Dirac basis element. To reduce unnecessary clutter,

everything on the right-hand side is put into the quantity $\tilde{K}_{(i),(j)}(P)$, and a summation over equal indices is implicit (Einstein convention). Thus, the integral equation is transformed into an ordinary linear algebra problem with an intrinsic dependency on P :

$$\Psi_{(i)} = \tilde{K}_{(i),(j)}(P)\Psi_{(j)}. \quad (5.1.4)$$

To solve this equation, it is transformed into an artificial eigenvalue problem,

$$\Psi_{(i)} = \lambda(P^2)\tilde{K}_{(i),(j)}(P)\Psi_{(j)}, \quad (5.1.5)$$

and a line search along the P axis is carried out to identify the smallest $|P_{min}^2|$ with

$$\lambda(P_{min}^2) = 1. \quad (5.1.6)$$

This procedure can be used to obtain both the ground state and the discrete excitation spectrum [39].

The eigenvalue problem was solved with an iterative QR-algorithm. The basic idea of the algorithm is to find a series of eigenvalue-conserving similarity transformations for the matrix A ,

$$A_0 = A, A_1 = Q_1^{-1}A_0Q_1 \dots A_n = Q_n^{-1}A_{n-1}Q_n, \quad (5.1.7)$$

so that A_n converges to an upper triangular matrix where the eigenvalues can be read off the diagonal [58]. Applying a transformation to an upper Hessenberg matrix (triangular plus a sub-diagonal), balancing and using a technique called *implicit double-shift*, see [34] for an explicit implementation, the algorithm finds all eigenvalues including the complex-conjugated pairs without using complex arithmetic.

To be able to use this well established algorithm, another obstacle has to be overcome. The kernel used in the meson and tetraquark BSE could be in principle complex and therefore needs a special treatment. Expanding the matrix equation $Ax = \lambda x$, with the assumption that $\lambda \in \mathbb{R}$ holds, and collecting purely imaginary and real parts together, the conversion to the following equivalent formulation $\hat{A}\hat{x} = \lambda\hat{x}$ is applicable:

$$\begin{pmatrix} A_{Re}^{11} & -A_{Im}^{11} & \cdots & -A_{Im}^{1n} \\ A_{Im}^{11} & A_{Re}^{11} & & \vdots \\ \vdots & & \ddots & \vdots \\ A_{Im}^{n1} & \cdots & \cdots & A_{Im}^{nn} \end{pmatrix} \begin{pmatrix} x_{Re}^1 \\ x_{Im}^1 \\ \vdots \\ x_{Im}^n \end{pmatrix} = \lambda \begin{pmatrix} x_{Re}^1 \\ x_{Im}^1 \\ \vdots \\ x_{Im}^n \end{pmatrix}. \quad (5.1.8)$$

Im and Re represent the imaginary and real part of the denoted variables. Without giving a proof, it turned out that even if the eigenvalues of A have a non-vanishing imaginary part, the eigenvalue spectrum of \hat{A} contains the spectrum of A . Because the dimensions of the matrix \hat{A} are doubled, it features twice as many eigenvalues as A . These 'additional' eigenvalues turned out to be the complex conjugated eigenvalues of A . When the eigenvalues of A are all real or occur in complex conjugated pairs, the eigenvalue spectrum of \hat{A} is effectively the doubled one of A . Furthermore the doubling of the matrix dimension did not significantly increase the computation time because the bulk of computation time is spent on calculating the multidimensional integrals of the kernel.

The calculation was done on a 12 core machine and took 20 to 40 minutes per iteration in the tetraquark case. The angular integration was carried out by means of the Smolyak algorithm, see the next chapter, and the momentum integration over (q, q'') used a 20-point Gauss-Legendre integration scheme on a logarithmic grid.

It may be noted that, when taking the remaining third Dirac basis element of the meson and diquark amplitudes into account, the kernel of the tetraquark BSE gets immensely huge when using *FeynCalc* (a few thousand lines). A possible cure to reduce the length of the kernel is to explicitly calculate the matrix multiplications and taking the trace during runtime. Multiplying eight matrices is considerable cheaper than adding thousands of scalar products that were produced by taking the trace beforehand with *FeynCalc* [59]. Because of the smallness of the third and fourth amplitude and the increasing numerical effort, only the first and second dominant meson/diquark amplitude was taken into account in this work.

5.2 Smolyak Integration

The kernels in the tetraquark BSE contain genuine two-loop graphs which feature six-dimensional integrals (one momentum-squared and five angular variables). Starting from the one dimensional quadrature formula as an approximation of the corresponding integral,

$$Q^n f := \sum_{i=0}^n w_i f(x_j), \quad (5.2.1)$$

with w_i being the weights and x_j the nodes of a quadrature method, for example a n th Gauss-Legendre quadrature that integrates all polynomial integrands of order $2n + 1$ exactly [58]. A d dimensional integral can be written as a tensor product

$$(Q_n \otimes \cdots \otimes Q_n)f := \sum_{i_1=0}^n \cdots \sum_{i_d=0}^n w_{i_1} \cdots w_{i_d} \cdot f(x_{i_1}, \dots, x_{i_d}). \quad (5.2.2)$$

It is immediately clear that the number of function evaluations grows exponentially with d . This renders the application of this approach to higher dimensional integrals very costly and is one example of the *curse of dimensionality*.

There exist methods to overcome this problem; for example the Monte-Carlo integration, which is based on the evaluation of the integrand on randomly generated points

$$\int dV f \approx \frac{V}{N} \sum_i^n f(X_i). \quad (5.2.3)$$

N denotes the total number of points and $X_i \in V$ is the i th random value. Another method is based on the Smolyak construction [60] for tensor products with the l th order Smolyak Quadrature in d dimensions Q_l^d given by

$$\begin{aligned} \Delta_k^1 f &:= (Q_k^1 - Q_{k-1}^1) f \\ Q_0^1 f &:= 0 \\ Q_l^d f &:= \sum_{\|\mathbf{k}\|_1 \leq l+d-1} (\Delta_{k_1}^1 \otimes \cdots \otimes \Delta_{k_d}^1) f = \\ &= \sum_{l \leq \|\mathbf{k}\|_1 \leq l+d-1} \binom{d-1}{\|\mathbf{k}\|_1 - 1} \cdot (Q_{k_1}^1 \otimes \cdots \otimes Q_{k_d}^1) f. \end{aligned} \quad (5.2.4)$$

$Q_l^1 f$ is a l th order one dimensional quadrature rule, for example Gauss-Legendre or Gauss-Chebyshev (Clenshaw-Curtis), and $\mathbf{k} \in \mathbb{N}^d$ holds. The evaluation points of the Smolyak quadrature form a d dimensional *sparse grid* that has for higher dimensions generally fewer evaluation points than the naive multi-dimensional quadrature, see Fig. 5.1 for an example of a sparse grid in 2 dimensions.

Instead of using a classical Gauss-Legendre quadrature, a nested Kronrod-Patterson extension [61] (higher order quadrature that contains points of the lower-order method), and furthermore minimizing the number of evaluation points, a method can be deduced that has for $d = 5$ a factor of ten less evaluation points than the naive Gauss-Legendre algorithm and integrates functions of polynomial order of less than $(2l - 1)$ exactly. The algorithm, proofs and further readings can be found in [62] and [63]. A Matlab-based program package calculating the weights and nodes for a prescribed accuracy and dimension is readily available [64] and was used.

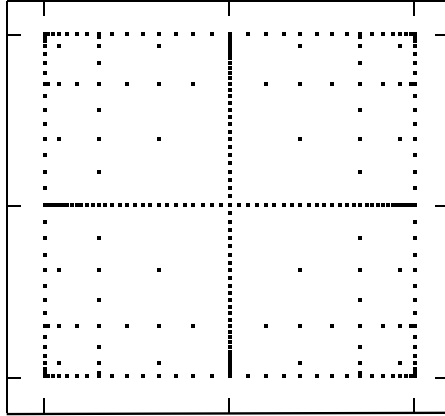


Figure 5.1: Sparse grid based on a Smolyak quadrature rule with $d = 2$ and $l = 8$. A Clenshaw-Curtis one dimensional quadrature is used as base.

The factor ten seems rather small but reduces the calculation time effectively by the same factor because the bottleneck of the whole calculation is the computation of the kernel. A further advantage of the Smolyak method in comparison to a Monte-Carlo method is the much better behavior when applied to oscillating functions. Testing both methods on very simple oscillating functions e.g. $f(x) = \sin(x) + \cos(y) + \sin(z)$ in three dimensions, the Smolyak method yields the correct result within the third digit, whereas the Monte Carlo method's result is way off. Because the nodes are known in advance, a precalculation of quantities that only depend on a subset of the integration variables is applicable.

The Smolyak construction applied for Chebyshev polynomials could also be used to reduce the grid size for interpolation problems in higher dimensions and might be of use in the calculation of the full tetraquark BSE where the amplitude depends on nine Lorentz invariants.

6 Results

In this chapter, the results for the $f_0(600)$ tetraquark are presented. The calculation was carried out in a Dyson-Schwinger/Bethe-Salpeter approach, employing a meson-meson/antidiquark-diquark picture for the tetraquark. The corresponding tetraquark Bethe-Salpeter equation is shown in Eq. (4.2.10). The input for these equations were the dressed quark propagator in rainbow-ladder truncation, calculated in chapter 2.3, and the offshell pion and scalar diquark amplitudes. The corresponding onshell BSEs were solved in chapter 3.7 and a consistent offshell prescription was introduced in chapter 3.5. In order to avoid an integration over the poles of the pion propagator, the tetraquark

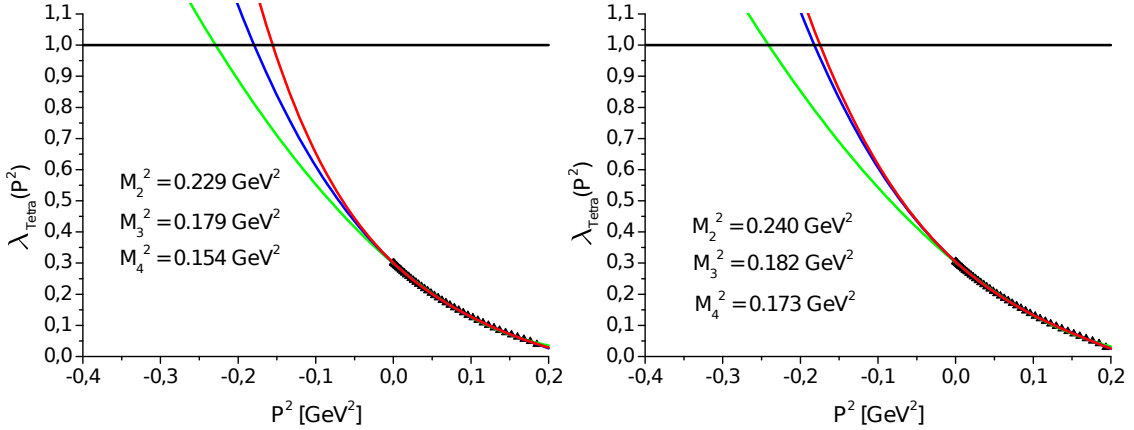


Figure 6.1: Eigenvalues of the tetraquark BSE as a function of the squared tetraquark momentum P^2 . The left plot shows the extrapolation of the Te1-N-D4T3 setup and the right one that of the Te2-N-D4T3. The abbreviations are explained in the text. Both setup give similar results, indicating that the dominant meson and diquark amplitudes give the major contribution to the mass.

BSE was solved for positive P^2 . Subsequently, the eigenvalue curve was extrapolated into the negative P^2 axis and the mass read off the intersection of the curve with one. Polynomials of order two, three and four were used as extrapolation functions, where the green colored curves in Figs. 6.1 - 6.3 denote second, the blue ones third and the red

ones fourth order polynomials.

A general problem that occurred for all setups, was the behavior for $P^2 \approx 0.2 \text{ GeV}^2$. The eigenvalue dipped below zero and showed an erratic jumping behavior, until for higher P^2 the eigenvalue crossed the 0-line again and approached zero asymptotically. The jumping behavior can be partly traced back to the eigenvalue algorithm that orders the eigenvalues after their (real) absolute value. Crossing the 0 can shift the hierarchy of the eigenvalues and make it difficult to find the 'correct' eigenvalue.

Furthermore, the dipping below 0 reminds of the problem with the prefactors $n(P^2)$ in Fig. (4.2.9) which also exhibit a zero crossing, leading to an ill-defined meson and diquark propagator. A possible reason for this behavior could be the offshell description of the meson and diquark.

The eigenvalue curve in the range of $[0; 0.2]$ is extrapolated into the negative P^2 -axis. Simple polynomials were used because it turned out that an extrapolation that applies irrational function fits did not work very well and could lead to an extrapolation *into* the singularities and not *away* from them. As extrapolants, polynomials of order two, three and four were used and the mass is given as the mean of the extrapolated values.

Notation

The abbreviations in Fig. 6.1 - 6.3 can be decrypted using the following notations: 'Te#' denotes how many basis elements of the meson and diquark amplitudes were taken into account when solving the tetraquark BSE. The subsequent character is $\in \{N, F, L\}$ and specifies the T-matrix ansatz and the method to handle the prefactors:

- The character 'N' specifies the T-matrix ansatz in Eq. (4.1.12) which only contains the product of the two-body T-matrices.
- The characters 'F' and 'Fl' apply the T-matrix ansatz of Eq. (4.1.11) containing additionally the single two-body T-matrices. In 'F' the diagram $n(P^2)$ is approximated by a best fit (irrational function of higher order) to obtain the prefactors and 'Fl' uses a simpler fit function (irrational function of order one).
- The setup denoted by 'L' uses the same ansatz for the T-matrix but utilizes the eigenvalue of the meson/diquark BSE to calculate the prefactors, see Eq. (4.4.6).

The final characters 'D#T#' denote the number of Dirac amplitudes (D) and Chebyshev moments (T) taken into account when solving the the meson and diquark BSE.

Setup (#)	Mass [GeV]
Te1-N-D4T3 (1)	0.433 ± 0.043
Te2-N-D4T3 (2)	0.445 ± 0.041
Te2-N-D2T1 (3)	0.464 ± 0.039
Te2-N-D4T3-MO (4)	$0.306^* \pm 0.042$
Te2-F-D4T3 (5)	0.326 ± 0.038
Te2-F1-D4T3 (6)	0.398 ± 0.038
Te2-L-D4T3 (7)	0.201 ± 0.013

Table 6.1: Tetraquark masses obtained from the different setups. The ending “MO“ denotes “mesons only“. The starred mass indicates that the sign of the T-matrix is reversed.

Dominant amplitudes

In setups (1-2), Fig. 6.1, the sensitivity of the tetraquark BSE on the number of Dirac components in the meson and diquark amplitude was investigated. Setup (1) truncated the amplitude of the meson and diquark *after* solving their corresponding BSEs to the dominant component ($\propto \mathbb{1}$). Setup (2) took the second amplitude ($\propto \not{P}$) into account as well. As can be seen in tab. 6.1, the mass changes only slightly when considering the error induced by the standard deviation of the three used extrapolating polynomials. This is no big surprise considering that the second meson and diquark amplitude is roughly a factor of ten smaller than the dominant one. The trend seems to be that the contribution of the second amplitudes shifts the mass to slightly higher values. In the light of the small influence of the second amplitude and the systematic errors introduced by the extrapolation procedure, the third one (\not{q}_T) was not considered but is expected to be of no great importance for the mass. The same is also expected for the fourth amplitude ($[\not{q}, \not{P}]$).

Influence of the truncation scheme

Setup (3), shown in Fig. 6.1, investigated the effect of a truncation of the BSE amplitude *before* solving the meson/diquark BSE. The resulting masses of the meson and diquark differ only a few percent from the untruncated values and the amplitudes also differ only in the 5% region. Plugging the amplitudes into the tetraquark BSE, the resulting tetraquark mass is roughly 5% away from the setups where the truncation was done afterwards. This difference can be put on the extrapolation routine and is still within the deviation of the result of setup (2). In summary, the mass of the tetraquark seems

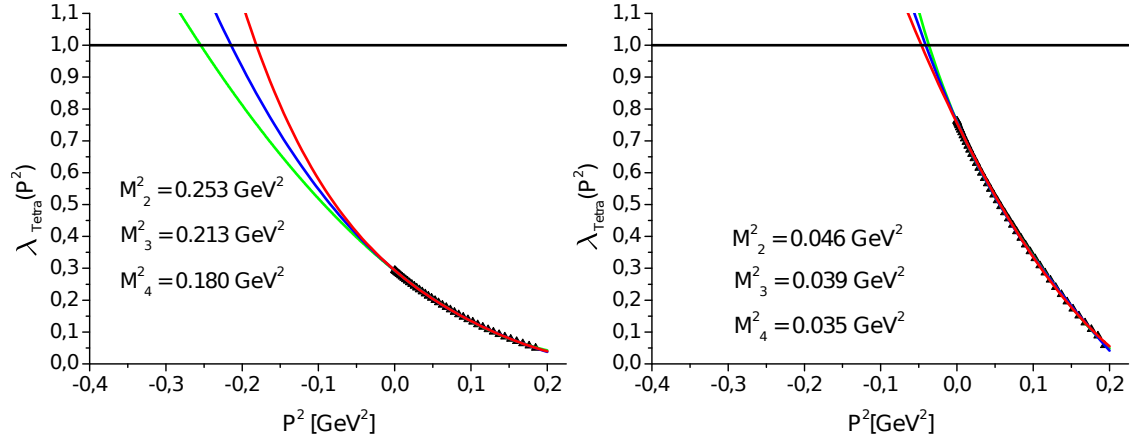


Figure 6.2: Eigenvalues of the tetraquark BSE as a function of the squared tetraquark momentum P^2 . The left plot shows the extrapolation of the T2-N-D2T1 setup and the right one that of T2-L-D4T3. See the text for explanations of the used abbreviations. The right setup explores the effect of calculating the prefactor from the meson eigenvalues. The left arrangement is similar to setup (2) except for the truncation scheme.

to be insensitive to the truncation scheme of the meson/diquark amplitudes.

Diquark contribution

Another feature that is prevalent throughout all setups which include meson-meson and antidiquark-diquark tetraquark amplitudes are the alternating eigenvalues of the BSE. The eigenvalue curves in Fig. 6.1-6.2 were deduced by the sign convention given in (4.1.12) and represent the highest positive eigenvalue. The second highest turned out to be always negative.

Applying this sign convention and switching off the antidiquark-diquark amplitude by setting it to zero in the tetraquark BSE, the resulting eigenvalue spectrum becomes *completely* negative which would imply that there is no bound state at all. Upon reversal of the sign, the spectrum changes sign and a mass was extrapolated, see setup (4) in tab. 6.1. This seems to indicate that there are subtle cancellations induced by the antidiquark-diquark contributions in the tetraquark BSE which are not resolved by a mere meson/meson approximation. Even upon sign reversal the mass of the meson-only setup is considerably smaller than the masses of the other setups.

This points out that the contribution from diquark/diquark correlations is of importance for the tetraquark as a bound state. To determine the influence of the diquark/diquark

correlations on a quantitative level, the tetraquark BSE has to be solved on mass-shell which could perhaps be achieved by solving Eq. (4.1.5) directly. .

Influence of Prefactors

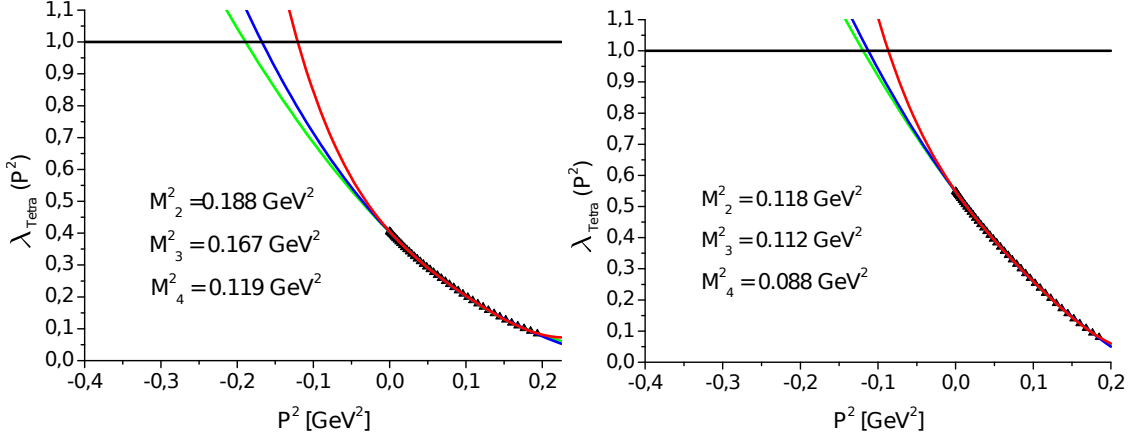


Figure 6.3: Eigenvalues of the tetraquark BSE as a function of the squared tetraquark momentum P^2 . The left plot shows the extrapolation of the T2-FI-D4T3 setup and the right one that of the T2-F-D4T3. See the text for explanations of the used abbreviations. In these setups the influence of the different fit approaches was tested.

Setups (5-6), see Fig. 6.3, applied the T-matrix ansatz of Eq. (4.1.11) which, apart from being more consistent in the sense that the T-matrix resembles the BSE kernel, has the major flaw that the emerging prefactors have singular parts, see chapter 4.4 for details. Both attempts to overcome the problem, which can be linked to the offshell description of the mesons, have their own flaws, too. The two setups that apply fits to the diagram $n(P^2)$ in Eq. (4.2.9) try to capture the decaying behavior of $n(P^2)$ and remove the zero crossing artificially by choosing appropriate fit functions. Setup (5) uses a function that fits the behavior before the crossing as good as possible which lead to terms of the form $(P^2)^5$ in the denominator. In conjunction with Eq. (4.4.1), this produces a prefactor α that behaves as a polynomial with the same order, see Fig. 4.7. If one assumes that the offshell description of the meson/diquark amplitudes is good (except for the zero crossing) and compares the α_n obtained by calculating the diagram $n(P^2)$, see Fig. 4.6, to the one obtained by the fit, a power behavior with higher powers than one seems unlikely. Unfortunately, this is the case when using the 'best' fit approach.

In view of this, a second fit function for setup (6) was used which qualitatively produced the expected (almost) linear behavior for high P^2 . This fit function, however, fits $n(P^2)$

in the region below the zero crossing much worse. Both setups lead to a reduction of the mass in comparison with setup (2), with setup (6) being the closest and within $\approx 10\%$ to the value of setup (2).

The conclusion that can be drawn is that the incorporation of the T-matrix ansatz of (4.1.11) results in a medium sized mass reduction, thus the main contribution to the mass of the tetraquark derives from the product of the two-body T-matrices. The reduction is roughly 10% for the low order fit and 25% for the 'best' fit. The discrepancy in the results for both fit ansätze shows that the exact form of the prefactors is important although, irrespective of the different power behavior of the prefactors, both setups indicate a bound-state mass in the region of 400 MeV.

In setup (7), see Fig. 6.2, the eigenvalue of the meson/diquark BSE is used to calculate the prefactor but the meson/diquark propagator inside the kernels utilizes the calculation of $n(P^2)$. Different than in the case of both setups using fits, the effect on the mass is much more drastic, yielding a mass of 200 MeV. Because this setup uses different approaches to calculate the prefactors on one hand and the meson/diquark propagators on the other hand, the large deviation is possibly caused by this inconsistency.

The mutual decrease in mass of setups (5-7) compared to (1-4) can be understood from the following consideration: The BSE is essentially handled as an eigenvalue problem $\lambda x = Kx$. When increasing the matrix K by multiplication of a factor bigger than 1, the eigenvalue is also increased. As seen in Fig. 4.7, the prefactors are ≥ 1 in all three setups for the major part between IR- and UV-cutoff. This shifts the eigenvalue curves to higher values, thus reducing the mass.

In summary, the existence of a low-mass solution for the 0^{++} tetraquark within the different setups seems to be a general feature, suggesting the existence of a tetraquark in the region of the σ meson. However, in view of the ambiguities that arise in the meson-meson/antidiquark-diquark simplification, further investigations from a genuine four-body bound-state equation would be desirable.

7 Conclusions and outlook

In this thesis the 0^{++} tetraquark mass was investigated in the covariant bound-state approach. Under the assumption that two-quark correlations are dominant, the four-quark bound-state equation simplifies to a coupled set of meson-meson and antidiquark-diquark Bethe-Salpeter equations. Upon retaining the lightest contributions in each channel, i.e., the pion and the scalar diquark, the resulting tetraquark equation was solved numerically.

The kernel of the tetraquark equation involves the dressed quark propagator as well as meson and diquark amplitudes and propagators. All ingredients were computed self-consistently in a rainbow-ladder truncation which traces the binding of two quarks to a dressed gluon exchange.

An offshell continuation of the onshell meson and diquark amplitudes was applied and the tetraquark BSE was solved for positive P^2 due to restrictions by the inherent pion poles.

To solve the multi-dimensional integration and reduce the numerical effort, a Smolyak integration routine was used. The mass of the tetraquark was then deduced by polynomial extrapolation of the eigenvalue curve into the negative P^2 region. Different setups were tested that explored the influence of the dominant and subdominant amplitudes on the mass. Furthermore, a comparison of different ansätze for the singular prefactors that emerged in the derivation of the two-body equation was carried out and the effect of the diquark/antidiquark contribution to the tetraquark amplitude was investigated.

The results for the ansatz that ignores the singular prefactors entirely found an extrapolated mass of roughly 450 MeV which is in the bounds of the experimental value for the σ . As expected, the influence of the subdominant amplitude is small and in the 10% region. The contribution of the antidiquark-diquark amplitude was found to be of great importance for the mass generation. The influence of the prefactors, employing three different ansätze to circumvent the singularity of the prefactors, turned out to reduce the mass qualitatively but the quantitative effect is unclear. Still, the existence of a low-mass solution is prevalent through all tested cases, indicating that the rainbow-ladder truncation gives rise to a $f_0(600)$ as tetraquark.

The problem of the singularities in the pion propagators could be mended by taking into account the pole via residuum calculus but the problem of the singular prefactors remains. In that respect, a direct solution of the four-body problem is desirable: it would solve all of the above mentioned problems could be extended to other quantum numbers as well.

8 Appendix

8.1 Chebyshev polynomials

The expansion in Chebyshev polynomials of the second kind uses the following relations which can be found in [65]. They are the basis solution of the differential equation

$$(1 - x^2) \frac{d^2 U(x)}{dx^2} - 3x \frac{dU(x)}{dx} + n(n + 2)U(x) = 0, \quad (8.1.1)$$

where n specifies the order of the polynomial. The first polynomials read

$$U_n(x) \in \{1, 2x, 4x^2 - 1, 8x^2 - 4x, \dots\}. \quad (8.1.2)$$

The projection of a function $f(x)$ on the Chebyshev polynomials is done by using the discrete version for the expansion coefficients:

$$u_n \approx \sum_{n=1}^N \frac{2(1 - x_n^2)}{N + 1} U_n(x_n) f(x_n), \quad x_n = \cos\left(\frac{\pi n}{N + 1}\right), \quad (8.1.3)$$

with the following representation of $f(x)$:

$$f(x) \approx \sum_{n=1}^{N'} u_n U_n(x). \quad (8.1.4)$$

The ' \approx ' points out that the applied expansion is only exact if carried out for infinite N' . Generally, $N > N'$ should hold; to reduce the calculation effort, $N := N' + 1$ was chosen throughout this work.

8.2 Euclidean conventions

In the following representation for the γ -matrices, with $k \in \{1, 2, 3\}$, the following one was chosen:

$$\gamma^k = \begin{pmatrix} 0 & -i\sigma^k \\ i\sigma^k & 0 \end{pmatrix}, \gamma^4 = \begin{pmatrix} \mathbb{1} & 0 \\ 0 & -\mathbb{1} \end{pmatrix}, \gamma_5 = \begin{pmatrix} 0 & \mathbb{1} \\ \mathbb{1} & 0 \end{pmatrix} \quad (8.2.1)$$

$$\{\gamma^\nu, \gamma^\mu\} = 2\delta^{\mu\nu}, \{\gamma^\nu, \gamma_5\} = 0. \quad (8.2.2)$$

The matrix γ^4 plays the role of γ^0 in Minkowski space. The charge conjugation matrix $\mathcal{C} = \gamma^4\gamma^2$ obeys the relations

$$\mathcal{C}^T = -\mathcal{C} = \mathcal{C}^{-1}. \quad (8.2.3)$$

The components of the Dirac vector $\not{p} = \gamma^\mu p_\mu$ are expressed in hyperspherical coordinates:

$$p^\mu = \sqrt{p^2} \begin{pmatrix} \sin(\theta) \sin \Psi \sin \Phi \\ \sin(\theta) \sin \Psi \cos \Phi \\ \sin(\theta) \cos \Psi \\ \cos(\theta) \end{pmatrix}. \quad (8.2.4)$$

9 Acknowledgements

I want to thank Christian Fischer and Gernot Eichmann for all the help and assistance throughout this work. Whenever there was a problem, they provided the knowledge, patience and time to discuss it. Especially, I want to thank Gernot for the thorough correction work on this thesis.

Also, I want to thank Jaqueline and Marcel for their help and fellowship. Last but not least, I want to thank my family for all their care and support.

Literaturverzeichnis

- [1] M. Gell-Mann, *Phys.Lett.* **8**, 214–215, 1964, [http://dx.doi.org/10.1016/S0031-9163\(64\)92001-3](http://dx.doi.org/10.1016/S0031-9163(64)92001-3).
- [2] R. Jaffe, *Phys.Rept.* **409**, 1–45, 2005, <http://dx.doi.org/10.1016/j.physrep.2004.11.005>.
- [3] I. Caprini, G. Colangelo, H. Leutwyler, *Phys.Rev.Lett.* **96**, 132001, 2006, <http://dx.doi.org/10.1103/PhysRevLett.96.132001>.
- [4] M. Ablikim, et al. (BES Collaboration), *Phys.Lett.* **B598**, 149–158, 2004, <http://dx.doi.org/10.1016/j.physletb.2004.07.052>.
- [5] K. Nakamura, et al. (PDG), *Note on scalar mesons*, 2010, <http://pdg.lbl.gov/2011/reviews/rpp2011-rev-scalar-mesons.pdf>.
- [6] R. Garcia-Martin, R. Kaminski, J. Pelaez, J. Ruiz de Elvira, *Phys.Rev.Lett.* **107**, 072001, 2011, <http://dx.doi.org/10.1103/PhysRevLett.107.072001>.
- [7] R. L. Jaffe, *Phys.Rev.* **D15**, 267, 1977, <http://dx.doi.org/10.1103/PhysRevD.15.267>.
- [8] E. Santopinto, G. Galata, *Phys.Rev.* **C75**, 045206, 2007, <http://dx.doi.org/10.1103/PhysRevC.75.045206>.
- [9] J. J. Dudek, R. G. Edwards, M. J. Peardon, D. G. Richards, C. E. Thomas, *Phys.Rev.* **D82**, 034508, 2010, <http://dx.doi.org/10.1103/PhysRevD.82.034508>.
- [10] K. Nakamura, et al. (PDG), *Journal of Physics* **G37**, 075021, 2010.
- [11] J. Iizuka, K. Okada, O. Shito, *Prog.Theor.Phys.* **35**, 1061–1073, 1966.
- [12] S. Okubo, *Phys.Lett.* **5**, 165–168, 1963, [http://dx.doi.org/10.1016/S0375-9601\(63\)92548-9](http://dx.doi.org/10.1016/S0375-9601(63)92548-9).

-
- [13] G. Zweig, An SU(3) model for strong interaction symmetry and its breaking. 2., Rep. TH-412, CERN, 1964.
- [14] N. Mathur, A. Alexandru, Y. Chen, S. Dong, T. Draper, et al., *Phys.Rev.* **D76**, 114505, 2007, <http://dx.doi.org/10.1103/PhysRevD.76.114505>.
- [15] M. Alford, R. Jaffe, *AIP Conf.Proc.* **688**, 208–219, 2004, <http://dx.doi.org/10.1063/1.1632207>.
- [16] S. Prelovsek, *Acta Phys.Polon.Supp.* **3**, 975–982, *Temporary entry*, 2010.
- [17] P. Maris, C. D. Roberts, *Int.J.Mod.Phys.* **E12**, 297–365, 2003, <http://dx.doi.org/10.1142/S0218301303001326>.
- [18] C. S. Fischer, *J.Phys.G* **G32**, R253–R291, 2006, <http://dx.doi.org/10.1088/0954-3899/32/8/R02>.
- [19] P. Maris, C. D. Roberts, *Phys.Rev.* **C56**, 3369–3383, 1997, <http://dx.doi.org/10.1103/PhysRevC.56.3369>.
- [20] D. Nicmorus, G. Eichmann, A. Krassnigg, R. Alkofer, *Phys.Rev.* **D80**, 054028, 2009, <http://dx.doi.org/10.1103/PhysRevD.80.054028>.
- [21] G. Eichmann, A. Krassnigg, M. Schwinzerl, R. Alkofer, *Annals Phys.* **323**, 2505–2553, 2008, <http://dx.doi.org/10.1016/j.aop.2008.02.007>.
- [22] M. Oettel, R. Alkofer, L. von Smekal, *Eur.Phys.J.* **A8**, 553–566, 2000, <http://dx.doi.org/10.1007/s100500070078>.
- [23] H. Georgi, *Lie algebras in particle physics*, Westview Press, 2nd ed., 1999.
- [24] L. Faddeev, V. Popov, *Phys.Lett.* **B25**, 29–30, 1967, [http://dx.doi.org/10.1016/0370-2693\(67\)90067-6](http://dx.doi.org/10.1016/0370-2693(67)90067-6).
- [25] M. Srednicki, *Quantum Field Theory*, Cambridge University Press, 2nd ed., 2007.
- [26] C. Itzikson, J. Zuber, *Quantum field theory*, Mc Graw and Hill, 5th ed., 1980.
- [27] F. Dyson, *Phys.Rev.* **75**, 1736–1755, 1949, <http://dx.doi.org/10.1103/PhysRev.75.1736>.
- [28] J. S. Schwinger, *Proc.Nat.Acad.Sci.* **37**, 452–455, 1951.

-
- [29] R. Alkofer, M. Q. Huber, K. Schwenzer, *Comput.Phys.Commun.* **180**, 965–976, 2009, <http://dx.doi.org/10.1016/j.cpc.2008.12.009>.
- [30] R. Alkofer, C. S. Fischer, F. J. Llanes-Estrada, K. Schwenzer, *Annals Phys.* **324**, 106–172, 2009, <http://dx.doi.org/10.1016/j.aop.2008.07.001>.
- [31] C. S. Fischer, R. Alkofer, *Phys. Rev.* **D67(9)**, 094020, 2003, <http://dx.doi.org/10.1103/PhysRevD.67.094020>.
- [32] P. Ramond, *Field Theory: A modern primer*, Addison-Wesley, 2nd ed., 1995.
- [33] P. Maris, P. C. Tandy, *Phys. Rev.* **C60(5)**, 055214, 1999, <http://dx.doi.org/10.1103/PhysRevC.60.055214>.
- [34] W. Press, S. Teukolsky, W. Vetterling, B. Flannery, *Numerical Recipes in C*, Cambridge University Press, 2nd ed., 1992.
- [35] *Openmp for c++*, <http://openmp.org/wp/>.
- [36] M. Oettel, R. Alkofer, *Eur. Phys. J.* **A16**, 95–109, 2003, <http://dx.doi.org/10.1140/epja/i2002-10070-4>.
- [37] C. S. Fischer, D. Nickel, R. Williams, *Eur.Phys.J.* **C60**, 47–61, 2009, <http://dx.doi.org/10.1140/epjc/s10052-008-0821-1>, [10.1140/epjc/s10052-008-0821-1](http://dx.doi.org/10.1140/epjc/s10052-008-0821-1).
- [38] G. Eichmann, *Hadron properties from QCD bound-state equations*, Ph.D. thesis, 2009, <http://arxiv.org/abs/0909.0703>.
- [39] A. Krassnigg, *PoS CONFINEMENT8*, 075, 2008.
- [40] C. Fischer, P. Watson, W. Cassing, *Phys.Rev.* **D72**, 094025, 2005, <http://dx.doi.org/10.1103/PhysRevD.72.094025>.
- [41] E. Salpeter, H. Bethe, *Phys.Rev.* **84**, 1232–1242, 1951, <http://dx.doi.org/10.1103/PhysRev.84.1232>.
- [42] Z. K. Silagadze, *Wick-Cutkosky model: An introduction*, 1998, <http://arxiv.org/abs/hep-ph/9803307>.
- [43] P. Maris, C. D. Roberts, P. C. Tandy, *Phys.Lett.* **B420**, 267–273, 1998, [http://dx.doi.org/10.1016/S0370-2693\(97\)01535-9](http://dx.doi.org/10.1016/S0370-2693(97)01535-9).

-
- [44] J. M. Cornwall, R. Jackiw, E. Tomboulis, *Phys.Rev.* **D10**, 2428–2445, 1974, <http://dx.doi.org/10.1103/PhysRevD.10.2428>.
- [45] D. W. McKay, H. J. Munczek, *Phys.Rev.* **D40**, 4151, 1989, <http://dx.doi.org/10.1103/PhysRevD.40.4151>.
- [46] P. Maris, P. Tandy, *Nucl.Phys.Proc.Suppl.* **161**, 136–152, 2006, <http://dx.doi.org/10.1016/j.nuclphysbps.2006.08.012>.
- [47] G. Eichmann, *Phys.Rev.* **D84**, 014014, 2011, <http://dx.doi.org/10.1103/PhysRevD.84.014014>.
- [48] D.Luri, A. Macfarlane, Y.Takahashi, *Phys.Rev.* **B140**, 1091–1099, 1965, <http://dx.doi.org/10.1103/PhysRev.140.B1091>.
- [49] N. Nakanishi, *Phys.Rev.* **138**, B1182–B1192, 1965, <http://dx.doi.org/10.1103/PhysRev.138.B1182>.
- [50] C. Llewellyn-Smith, *Annals Phys.* **53**, 521–558, 1969, [http://dx.doi.org/10.1016/0003-4916\(69\)90035-9](http://dx.doi.org/10.1016/0003-4916(69)90035-9).
- [51] M. Oettel, L. Von Smekal, R. Alkofer, *Comput.Phys.Commun.* **144**, 63, 2002, [http://dx.doi.org/10.1016/S0010-4655\(01\)00465-9](http://dx.doi.org/10.1016/S0010-4655(01)00465-9).
- [52] A. Bender, C. D. Roberts, L. Von Smekal, *Phys.Lett.* **B380**, 7–12, 1996, [http://dx.doi.org/10.1016/0370-2693\(96\)00372-3](http://dx.doi.org/10.1016/0370-2693(96)00372-3).
- [53] M. Bhagwat, A. Hoell, A. Krassnigg, C. Roberts, S. Wright, *Few Body Syst.* **40**, 209–235, 2007, <http://dx.doi.org/10.1007/s00601-007-0174-6>.
- [54] G. Eichmann, I. Cloet, R. Alkofer, A. Krassnigg, C. Roberts, *Phys.Rev.* **C79**, 012202, 2009, <http://dx.doi.org/10.1103/PhysRevC.79.012202>.
- [55] A. Khvedelidze, A. Kvinikhidze, *Theor.Math.Phys.* **90**, 62–74, 1992, <http://dx.doi.org/10.1007/BF01018820>.
- [56] K. Huang, H. A. Weldon, *Phys.Rev.* **D11**, 257, 1975, <http://dx.doi.org/10.1103/PhysRevD.11.257>.
- [57] *FeynCalc*, <http://www.feynCalc.org/>.
- [58] R. Freund, R. Hoppe, *Numerische Mathematik 1*, Springer, 10th ed., 2007.

-
- [59] R. Williams, *Bethe-Salpeter studies of mesons beyond rainbow-ladder*, 2009, <http://arxiv.org/pdf/0912.3494v1>.
- [60] S. Smolyak, *Dokl. Akad. Nauk SSSR* **4(240-243)**, 123, 1963.
- [61] T. Patterson, *Math. Comput* **22**, 847–856, 1968.
- [62] K. Petras, *Numerische Mathematik* **93(4)**, 729–753, 2003.
- [63] T. Gerstner, M. Griebel, *Numerical algorithms* **18(3)**, 209–232, 1998.
- [64] H. Florian, W. Viktor, *Journal of Econometrics* **144(1)**, 62–80, 2008, <http://sparse-grids.de/>, <http://dx.doi.org/10.1016/j.jeconom.2007.12.004>.
- [65] M. Abramowitz, I. A. Stegun, *Handbook of Mathematical Functions with Formulas, Graphs, and Mathematical Tables*, Dover, 9th ed., 1964.